Variational Multiscale Enrichment Method with Mixed Boundary Conditions for Modeling Diffusion and Deformation Problems

Caglar Oskay*

Department of Civil and Environmental Engineering
Vanderbilt University
Nashville, TN 37235

Abstract

This manuscript presents the formulation and implementation of the variational multiscale enrichment (VME) method using *canopy*-shaped microscale enrichment functions obtained through the use of a new family of microscale boundary conditions. The purpose of the new enrichment functions and the new boundary condition is to relax the overconstraint imposed by the homogeneous microscale boundary condition (e.g., residual free bubbles) commonly employed in the variational multiscale literature. The formulation and implementation of the method are presented for diffusion and elasticity problems. The performance of the proposed method is assessed by comparing with direct numerical simulations on diffusion and deformation problems. A boundary parameter identification approach is proposed to obtain near-optimal boundary conditions. The identification approach is verified in the context of the deformation response of particle-reinforced composites.

Keywords: Variational multiscale enrichment; Multiphysics; Boundary conditions, Diffusion, Elasticity.

1 Introduction

We are concerned with surface degradation problems that exhibit global-local character, in which an aggressive environmental agent (i.e., a fluid) diffuses into the surface region of a structure or material, significantly altering the mechanical response within this subdomain. Direct numerical simulation that incorporates all relevant fine scale details throughout the surface region is typically infeasible due to the prohibitive computational cost. On the other hand, phenomenological description within this local subdomain is not possible since the size

*Corresponding author address: VU Station B#351831, 2301 Vanderbilt Place, Nashville, TN 37235. Email: caglar.oskay@vanderbilt.edu

of the surface region may be smaller than the characteristic size of the representative volume defined by the microstructural heterogeneity.

Global-local methods attempt to capture the fine scale behavior at small subdomains of the problem, whereas a coarse description (e.g., a coarse discretization and phenomenological modeling) is employed at "far-field" regions. Some domain decomposition methods [1], s-version finite elements [2], generalized finite elements [3], among others are examples of global-local methods employing this idea. Variational multiscale method (VMM) is an alternative framework for incorporating fine scale response to an otherwise coarse representation [4, 5]. The key component of the VMM method is the additive decomposition of the response fields into coarse and fine scale components. The fine scale component is often evaluated analytically through variational projection as a function of the residual of the coarse scale field [6, 7]. This approach leads to an enriched coarse scale response, which can be evaluated without further regard to the localized response. It is also possible to evaluate the fine scale response numerically, which gave rise to the numerical subgrid upscaling method [8]. The numerical subgrid upscaling is more versatile compared to analytical projection operator for the fine scale, which may be nontrivial to obtain for nonlinear and path dependent problems. Yet, the computational cost of the method is significantly higher than the analytical projection methods. Arbogast [9] proposed computationally efficient subgrid upscaling schemes in the context of locally conservative porous media flow. Variational multiscale enrichment (VME) is a new VMM-based numerical subgrid method proposed for problems exhibiting global-local character [10]. The premise of the VME approach is that the enrichment of the coarse grid is considered at local subdomains, and the fine scale response fields are numerically computed at these small subdomains only.

The accuracy of the response approximation in such multiscale computational methods is significantly affected by the boundary conditions imposed on the fine scale problems. In the VMM literature, the typical choice for fine scale boundary conditions has been the homogeneous Dirichlet condition (i.e., residual free bubble functions [11, 12]). Recently, Juanes and Dub [13] proposed a relaxed constraint for the fine scale response fields in the context of the numerical subgrid upscaling scheme applied to porous media flow problems. Markovic and Ibrahimbegovic [14] imposed traction continuity across the fine scale problem interfaces. Hund and Ramm [15] investigated the effect of homogeneous conditions and enforcing displacement continuity in the context of localization problems. The displacement continuity was applied based on either the penalty method or Lagrange multipliers. The Lagrange multiplier method leads to the coupling of all neighboring fine scale domains and domain decomposition was employed to study the response. In case of the penalty method, the authors found that weak enforcement of the continuity through picking a low value for the penalty parameter led to accurate response. The present approach proposed in this manuscript is related to such a soft penalty approach. The choice of fine scale boundary conditions has been subject to investigations in other multiscale methods (e.g., computational homogenization) as well. In addition to most commonly employed boundary conditions of uniform Dirichlet, uniform Neumann and

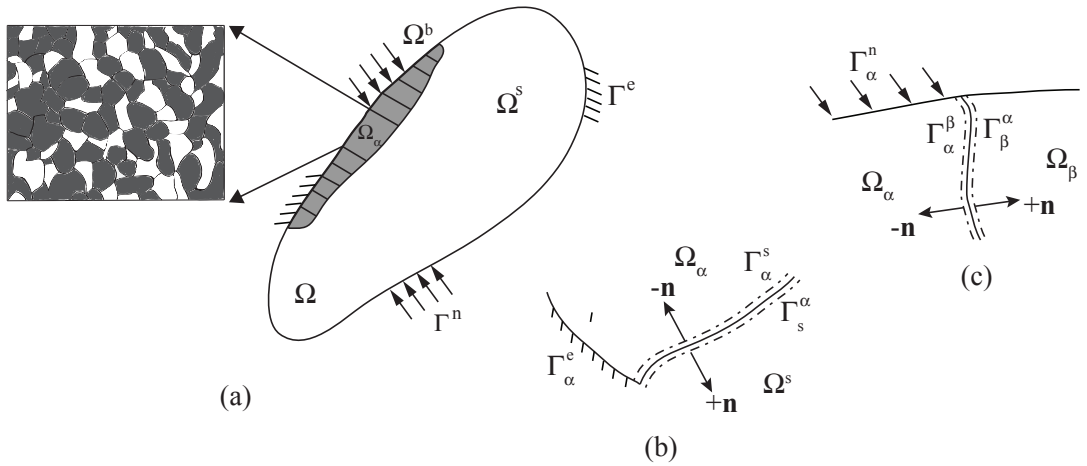

Figure 1: Problem geometry: (a) Schematic representation of the overall problem domain; (b) boundary between an enrichment domain and the substrate region; and, (c) boundary between two enrichment domains.

periodicity, new boundary conditions have been recently proposed to address large deformations [16], fracture phenomena [17] and plate assumptions [18]. Appropriate application of the coarse scale boundary conditions, a separate problem altogether, has also been investigated in the context of the VMM approach [19, 20].

In the present manuscript, we propose a new class of boundary conditions for the fine scale response in the context of the variational multiscale enrichment method. The resulting fine scale fields are named canopy functions (compare to the residual free bubbles) since the fine scale response is relaxed across coarse grid boundaries. The proposed boundary conditions are applied to the time dependent diffusion (parabolic) and elasticity (elliptic) problems to assess the accuracy characteristics. We also provide parametric studies to identify appropriate boundary conditions as a function of the physical parameters of the diffusion and elasticity problems.

The remainder of this manuscript is organized as follows: Section 2 provides the formulation of the variational multiscale enrichment method with canopy functions in the context of diffusion and deformation problems. Section 3 details the computational implementation of the method including the finite element discretization of fine and coarse scale problems, as well as the overall solution strategy. In Section 4, numerical examples are provided to verify the new boundary conditions. The performance of the variational multiscale enrichment method is studied on diffusion and deformation problems. Section 5 provides the conclusions and future research directions in this area.

2 Variational Multiscale Enrichment

Let the open bounded domain $\Omega \in \mathbb{R}^{n_{\text{sd}}}$ represent the structure or the material, where n_{sd} is the number of spatial dimensions (Fig 1). We consider the decomposition of the problem

domain into two characteristic subdomains:

$$\Omega = \Omega^s \cup \Omega^b; \quad \Omega^s \cap \Omega^b = \emptyset \tag{1}$$

in which, Ω^b and Ω^s are the boundary and substrate regions, respectively. The boundary region constitute the part of the problem domain in which the underlying heterogeneities of its microstructure as well as the response fields are resolved, whereas in the substrate region, the response is represented at the coarse scale only and the subgrid effects remain unresolved. From the physical perspective, the boundary region contains aggressive agent at critical concentrations, microcracks or fracture initiation sites. The boundary region is further divided into a number of enrichment domains, Ω_α:

$$\Omega^b = \bigcup_{\alpha=1}^{n_{\text{en}}} \Omega_\alpha; \quad \Omega_\alpha \cap \Omega_\beta \equiv \emptyset \text{ when } \alpha \neq \beta \tag{2}$$

where, n_{en} is the number of enrichment domains that span the boundary region. The enrichment domains, Ω_α are taken to be simple (i.e., representable using a single standard finite element such as a rectangular or triangular domain in 2-D). The boundary of an enrichment domain is composed of the following parts:

$$\Gamma_\alpha \equiv \partial\Omega_\alpha = \Gamma_\alpha^{\text{int}} \cup \Gamma_\alpha^s \cup \Gamma_\alpha^e \cup \Gamma_\alpha^n \tag{3}$$

in which, Γ_α^s is the part of the boundary that intersects with the substrate region boundary (i.e., $\Gamma_\alpha^s \equiv \Gamma_\alpha \cap \partial\Omega^s$) as illustrated in Fig. 1b; Γ_α^e the part of the boundary that intersects with the Dirichlet boundary of the problem domain (i.e., $\Gamma_\alpha^e \equiv \Gamma_\alpha \cap \Gamma^e$); Γ_α^n the part of the boundary that intersects with the Neumann boundary of the problem domain (i.e., $\Gamma_\alpha^n \equiv \Gamma_\alpha \cap \Gamma^n$); and, $\Gamma_\alpha^{\text{int}}$ the inter-enrichment domain boundaries:

$$\Gamma_\alpha^{\text{int}} \equiv \bigcup_{\beta \in I_\alpha} \Gamma_\alpha^\beta \tag{4}$$

where, the neighbor index set of enrichment domain, Ω_α, is expressed as: $I_\alpha \equiv \{\beta \leq n_{\text{en}} | \Gamma_{\alpha\beta} \neq \emptyset\}$. $\Gamma_{\alpha\beta}$ denotes the inter-enrichment domain boundary (i.e., $\Gamma_{\alpha\beta} \equiv \Gamma_\alpha \cap \Gamma_\beta$); and, Γ_α^β and Γ_β^α denote the α and β sides of the inter-enrichment domain boundary, respectively, as illustrated in Fig. 1(c).

2.1 Diffusion problem

The diffusion process is modeled using the following equation:

$$\dot{c}(\mathbf{x}, t) = \nabla \cdot [\mathbf{D}(\mathbf{x}, t) \cdot \nabla c(\mathbf{x}, t)]; \quad \mathbf{x} \in \Omega \tag{5}$$

in which, c denotes the concentration field; $\mathbf{D}$ the apparent diffusivity; $\mathbf{x}$ the position coordinate vector; and, $t \in \mathcal{T} \subset \mathbb{R}^+$ the time coordinate. Superposed dot denotes the time derivative of the corresponding field. The boundary and initial conditions are:

$$\text{Dirichlet B.C.:} \qquad c(\mathbf{x},t) = \tilde{c}(\mathbf{x},t); \quad \mathbf{x} \in \Gamma^c \tag{6}$$

$$\text{Neumann B.C.:} \qquad \mathbf{D} \cdot \nabla c \cdot \mathbf{n} = \tilde{q}(\mathbf{x},t); \quad \mathbf{x} \in \Gamma^q \tag{7}$$

$$\text{Initial condition:} \qquad c(\mathbf{x}, t=0) = c_0(\mathbf{x}); \quad \mathbf{x} \in \Omega \tag{8}$$

where, $\tilde{c}$ and $\tilde{q}$ the prescribed Dirichlet and Neumann boundary data along the domain boundary $\Gamma \equiv \partial\Omega$, respectively (i.e., $\Gamma^e = \Gamma^c$ and $\Gamma^n = \Gamma^q$ such that $\Gamma^c \cup \Gamma^q = \Gamma$ and $\Gamma^c \cap \Gamma^q = \emptyset$); c_0 the prescribed initial concentration distribution; and $\mathbf{n}$ the unit outward normal to the domain boundary.

We start by considering the following decomposition of the concentration field:

$$c(\mathbf{x},t) = c^M(\mathbf{x},t) + \sum_{\alpha=1}^{n_{\text{en}}} \mathcal{H}(\Omega_\alpha)\, c_\alpha^m(\mathbf{x},t) \tag{9}$$

where, c^M denotes a coarse scale representation of the response field; and c_α^m a fine scale correction to the coarse scale approximation localized within an enrichment domain, Ω_α:

$$\mathcal{H}(\Omega_\alpha) = \begin{cases} 1 & \text{if } \mathbf{x} \in \Omega_\alpha \\ 0 & \text{elsewhere} \end{cases} \tag{10}$$

The decomposition of the concentration field is applied to the diffusion problem in the variational setting. Introducing a macroscale test function $v^M \in \mathcal{W}_0^M \subset H_0^1(\Omega)$, and substituting Eq. 9 into Eq. 5, the following macroscale diffusion problem is obtained in the weak form:

$$a\left(v^M, c^M\right)_\Omega^c + \left(v^M, \dot{c}^M\right)_\Omega^c = \left(v^M, \tilde{q}\right)_{\Gamma^q}^c + \sum_{\alpha=1}^{n_{\text{en}}} \left[\left(v^M, q_\alpha^m\right)_{\Gamma_\alpha \setminus \Gamma}^c - a\left(v^M, c_\alpha^m\right)_{\Omega_\alpha}^c - \left(v^M, \dot{c}_\alpha^m\right)_{\Omega_\alpha}^c\right] \tag{11}$$

where, $q_\alpha^m = \mathbf{D} \cdot \nabla c_\alpha^m \cdot \mathbf{n}$ is the microscale flux normal to the enrichment domain boundary; $H_0^1(\Omega)$ is the subspace of functions in $H^1(\Omega)$ that are homogeneous along $\Gamma^e = \Gamma^c$, and $H^1(\Omega)$ is the Sobolev space of functions with square integrable values and derivatives defined within the problem domain. In what follows, a subscript of a function space indicates the prescribed value of the functions along the Dirichlet boundaries (e.g., $H_g^1(\Omega) := \left\{u \in H^1(\Omega) \,|\, u = g;\ \mathbf{x} \in \Gamma^e\right\}$). The bilinear form and the L_2 inner product for the diffusion

problem are, respectively:

$$a\left(u,w\right)^{c}_{[\cdot]} \equiv \int_{[\cdot]} \nabla u \cdot \mathbf{D} \cdot \nabla w \, d[\cdot] \tag{12}$$

$$\left(u,w\right)^{c}_{[\cdot]} \equiv \int_{[\cdot]} u \, w \, d[\cdot] \tag{13}$$

We seek the solution to Eq. 11 in the finite dimensional space $\mathcal{W}^{M}_{\tilde{c}^{M}}\left(\Omega\right) \subset H^{1}_{\tilde{c}^{M}}\left(\Omega\right)$, where $\tilde{c}^{M}$ denotes the approximation of the boundary data using the macroscale basis functions that are taken to span a coarse discretization of the domain. The microstructural heterogeneities remain unresolved at this scale.

The effect of the microstructure are resolved using the microscale response, c^{m}_{α}, which is taken to be localized within an enrichment domain, Ω_{α} in view of the decomposition of Eq. 9. The solution of the microscale response fields is sought within the finite dimensional subspace $\mathcal{W}_{\alpha,\tilde{c}_{\alpha}}\left(\Omega_{\alpha}\right) \subset H^{1}_{\tilde{c}_{\alpha}}\left(\Omega_{\alpha}\right)$. Considering a microscale test function, $v^{m}_{\alpha} = \mathcal{W}_{\alpha,0}\left(\Omega_{\alpha}\right)$, and bringing Eq. 5 into the weak form yields the microscale diffusion problem for the enrichment domain, Ω_{α}:

$$a\left(v^{m}_{\alpha},c^{m}_{\alpha}\right)^{c}_{\Omega_{\alpha}} + \left(v^{m}_{\alpha},\dot{c}^{m}_{\alpha}\right)^{c}_{\Omega_{\alpha}} = \left(v^{m}_{\alpha},q^{M}\right)^{c}_{\Gamma_{\alpha}\setminus\Gamma^{c}_{\alpha}} + \left(v^{m}_{\alpha},q^{m}_{\alpha}\right)^{c}_{\Gamma_{\alpha}\setminus\Gamma^{c}_{\alpha}} - a\left(v^{m}_{\alpha},c^{M}\right)^{c}_{\Omega_{\alpha}} - \left(v^{m}_{\alpha},\dot{c}^{M}\right)^{c}_{\Omega_{\alpha}} \tag{14}$$

in which, $q^{M} = \mathbf{D}\cdot\nabla c^{M}\cdot\mathbf{n}$ is the macroscale flux normal to the enrichment domain boundary.

Remark 1. *The decomposition of Eq. 9 is unique if the macro- and microscale solution spaces are chosen such that the solution space is the direct sum of the macro- and microscale spaces:*

$$\mathcal{W}_{\tilde{q}}\left(\Omega\right) = \mathcal{W}^{M}_{\tilde{q}^{M}}\left(\Omega\right) \oplus \bigoplus_{\alpha=1}^{n_{\text{en}}} \mathcal{W}_{\alpha,\tilde{q}_{\alpha}}\left(\Omega_{\alpha}\right) \tag{15}$$

$c \in \mathcal{W}_{\tilde{q}}\left(\Omega\right)$. It suffices to show that the macroscale and each microscale finite dimensional subspace are pairwise linearly independent. By virtue of the concentration decomposition, the microscale contributions within the enrichment domains are linearly independent of each other.

2.1.1 Boundary conditions for the microscale enrichment fields:

The standard choice for the boundary conditions of the microscale response is the homogeneous Dirichlet conditions ($c^{m}_{\alpha} = 0$) along the entire enrichment domain boundary. The resulting microscale solution field is a residual free bubble introduced in Refs. [11, 12, 21]. Figure 2a schematically illustrates a residual-free bubble (RFB) enrichment function. Previous investigations on diffusion and elasticity problems using the VME method indicated that employing homogeneous boundary conditions leads to stiff response and relatively low solution accuracy [10]. In this manuscript, we propose a new type of boundary conditions to reduce the modeling errors that originate from overconstraining the enrichment domain boundaries. To

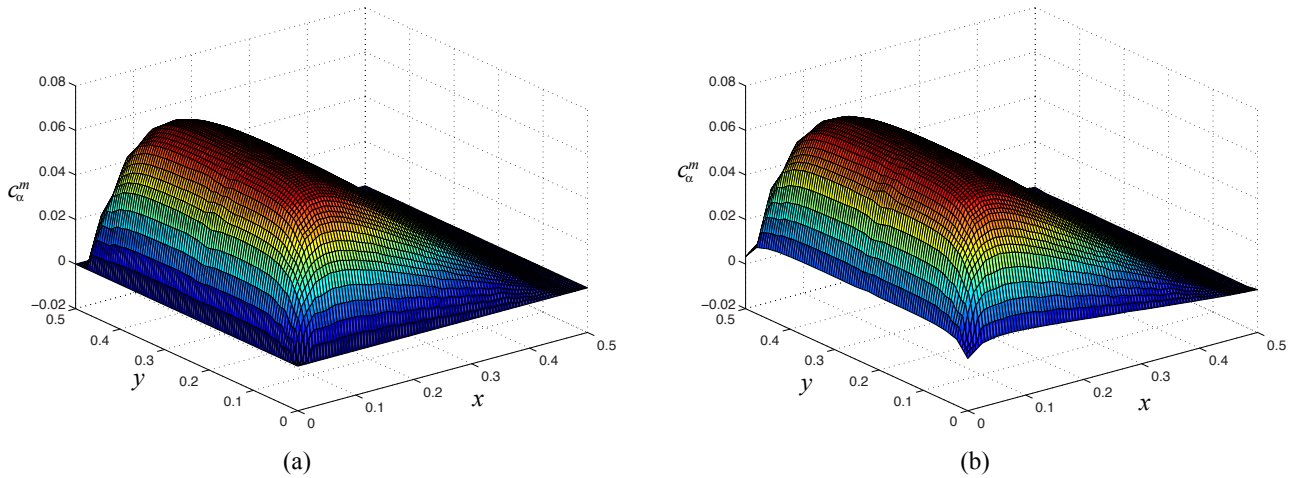

Figure 2: Schematic illustration of the microscale enrichment functions defined in an enrichment domain: (a) Residual free bubble functions; and (b) Canopy functions.

this extent, the following constraint at the enrichment domain boundaries is considered:

$$\theta\left(c_\alpha^m - \hat{c}_\alpha\right) + (1-\theta)^\gamma\left(q_\alpha^m - \hat{q}_\alpha\right) = 0; \quad \mathbf{x} \in \Gamma_\alpha \tag{16}$$

This family of boundary conditions spans the two microscopic boundary conditions commonly employed in multiscale modeling: prescribed flux and prescribed concentration along the microscale boundaries. The prescribed flux (Neumann) boundary condition is imposed by setting $\theta = 0$, whereas prescribed concentration (Dirichlet) boundary condition is imposed by setting $\theta = 1$. All intermediate values $0 < \theta < 1$ correspond to a mixed (Robin) boundary condition. The purpose of the γ parameter is to increase the sensitivity of the response to the boundary parameter, θ, around the prescribed concentration limit (i.e., $\theta \to 1$). The residual free bubble functions for the microscale fields can be constructed by setting $\theta = 1$ and $\hat{c}_\alpha = 0$ along Γ_α.

Equation 16 is expressed in terms of a single parameter, κ, as:

$$q_\alpha^m = \hat{q}_\alpha - \kappa\left(c_\alpha^m - \hat{c}_\alpha\right) \tag{17}$$

where, $\kappa = \theta/(1-\theta)^\gamma$. By setting the boundary parameter, $0 \leq \kappa < \infty$, the boundary response is relaxed along the edges of the enrichment domain. The microscale concentration at the corners of the enrichment domains is set to zero. This constraint ensures that: (1) when micro- and macroscale discretizations are nested (described below) and when Lagrangian (standard) finite elements are employed, the nodal values obtained through the evaluation of the macroscale equation correspond to the concentration values (i.e., the nodal values approximates the response field, c); and (2) the zero energy modes of the microscale response are constrained. The resulting microscale enrichment field (canopy functions) is schematically illustrated in Fig. 2b.

The new boundary condition defined in Eq. 17 is applied to the microscale and macroscale

diffusion problems. The boundary terms in the microscale diffusion problem (Eq. 14) is decomposed into the boundary components defined in Eq. 3:

$$(v_\alpha^m, q_\alpha^m)^c_{\Gamma_\alpha \setminus \Gamma_\alpha^c} = (v_\alpha^m, q_\alpha^m)^c_{\Gamma_\alpha^q} + (v_\alpha^m, q_\alpha^m)^c_{\Gamma_\alpha^{\text{int}}} + (v_\alpha^m, q_\alpha^m)^c_{\Gamma_\alpha^s} \tag{18}$$

Along the boundaries of the enrichment domain that intersects with the outer boundaries with Neumann boundary conditions (i.e., Γ_α^q), the microscale flux field is defined as the difference between the prescribed boundary flux (i.e., $\tilde{q}$), and the approximation to the flux field based on the macroscale discretization. Setting $\theta = 0$ and $\hat{q}_\alpha = \tilde{q}_\alpha := \tilde{q} - \tilde{q}^M$, where $\tilde{q}^M$ is the approximation to the prescribed boundary data using the macroscale discretization:

$$(v_\alpha^m, q_\alpha^m)^c_{\Gamma_\alpha^q} = (v_\alpha^m, \tilde{q}_\alpha)^c_{\Gamma_\alpha^q} \tag{19}$$

Along the inter-enrichment domain boundaries (i.e., $\Gamma_\alpha^{\text{int}}$), the boundary term in its general form becomes:

$$(v_\alpha^m, q_\alpha^m)^c_{\Gamma_\alpha^{\text{int}}} = \sum_{\beta \in I_\alpha} \left[(v_\alpha^m, \hat{q}_\alpha)^c_{\Gamma_\alpha^\beta} - \kappa \, (v_\alpha^m, c_\alpha^m - \hat{c}_\alpha)^c_{\Gamma_\alpha^\beta} \right] \tag{20}$$

The limiting boundary conditions along the inter-enrichment boundaries are taken to vary from microscale flux free ($\hat{q}_\alpha = 0$) to vanishing microscale concentration ($\hat{c}_\alpha = 0$). Equation 20 then reduces to:

$$(v_\alpha^m, q_\alpha^m)^c_{\Gamma_\alpha^{\text{int}}} = - \sum_{\beta \in I_\alpha} \kappa \, (v_\alpha^m, c_\alpha^m)^c_{\Gamma_\alpha^\beta} \tag{21}$$

For a given value of the boundary parameter, $0 < \kappa < \infty$, the resulting enrichment domain boundary response leads to non-zero microscale flux and microscale concentrations. Along the boundaries of the enrichment domain that intersects with the substrate region (i.e., Γ_α^s), the boundary term is expressed as:

$$(v_\alpha^m, q_\alpha^m)^c_{\Gamma_\alpha^s} = -\kappa_s \, (v_\alpha^m, c_\alpha^m)^c_{\Gamma_\alpha^s} \tag{22}$$

when the flux free and concentration free boundaries are taken as the limiting microscale boundary conditions. It is possible to satisfy the continuity of the concentration field across the subgrid resolved (i.e., boundary) and the subgrid unresolved (i.e., substrate) regions by setting $\kappa_s \to \infty$, which ensures homogeneous microscale response along the boundary regions - substrate region interface. Applying this boundary condition induces flux discontinuity at the microscale, since the microscale flux field along the substrate remains unresolved. In contrast, setting $\kappa_s = 0$ ensures continuity of the fluxes by insulating the microscale concentration field at the interface. Applying $\kappa_s = 0$ induces concentration discontinuity at the microscale, since the microscale concentration along the substrate remains unresolved. Numerical investigations indicated higher accuracy is achieved when a mixed boundary condition is adopted along the boundary region - substrate region interface as well. In this manuscript we set the boundary parameter, $\kappa_s = \kappa$. By this condition, both microscale concentration and flux continuities are

relaxed along the interface, but to a lesser extent than the limiting cases of $\kappa_s = 0$ and $\kappa_s = \infty$ conditions.

Substituting Eqs. 19-22 into Eq. 14, the weak form of the microscale diffusion problem is expressed as:

$$a\left(v_\alpha^m, c_\alpha^m\right)_{\Omega_\alpha}^c + \left(v_\alpha^m, \dot{c}_\alpha^m\right)_{\Omega_\alpha}^c = \left(v_\alpha^m, \tilde{q}_\alpha\right)_{\Gamma_\alpha^q}^c + \left(v_\alpha^m, q^M\right)_{\Gamma_\alpha}^c - \kappa\left(v_\alpha^m, c_\alpha^m\right)_{\Gamma_\alpha^s}^c - \sum_{\beta \in I_\alpha} \kappa\left(v_\alpha^m, c_\alpha^m\right)_{\Gamma_\alpha^\beta}^c - a\left(v_\alpha^m, c^M\right)_{\Omega_\alpha}^c - \left(v_\alpha^m, \dot{c}^M\right)_{\Omega_\alpha}^c \quad (23)$$

2.1.2 Inter-enrichment domain continuity:

Equation 23 permits discontinuity of the concentration field when the general form of the mixed boundary condition is imposed along the inter-enrichment domains. To satisfy the continuity of the concentration field across the inter-enrichment domain boundaries, we explicitly consider:

$$c_\alpha^m = c_\beta^m; \quad \mathbf{x} \in \Gamma_\alpha^\beta; \quad \forall \beta \in I_\alpha \quad (24)$$

The values of the concentration fields c_α^m and c_β^m are both unknown along the enrichment domain boundaries and cannot be readily enforced as boundary data. A master-slave coupling approach is employed to impose the field continuity along the inter-enrichment domain boundaries. Let the neighbor index set for the enrichment domain, α be split into a master and slave index sets such that:

$$I_\alpha^m \equiv \{\beta | \alpha < \beta \leq n_{\text{en}} \text{ and } \Gamma_{\alpha\beta} \neq \emptyset\}; \quad I_\alpha^s \equiv \{\beta | \beta < \alpha \leq n_{\text{en}} \text{ and } \Gamma_{\alpha\beta} \neq \emptyset\} \quad (25)$$

The inter-enrichment domain boundary term in Eq. 23 is expressed as:

$$\sum_{\beta \in I_\alpha} \kappa\left(v_\alpha^m, c_\alpha^m\right)_{\Gamma_\alpha^\beta}^c = \sum_{\beta \in I_\alpha^m} \kappa\left(v_\alpha^m, c_\alpha^m\right)_{\Gamma_\alpha^\beta}^c + \sum_{\beta \in I_\alpha^s} \kappa_\infty \left(v_\alpha^m, c_\alpha^m - c_\beta^m\right)_{\Gamma_\alpha^\beta}^c \quad (26)$$

in which, $\kappa_\infty \approx \infty$ acts as the penalty parameter and ensures that the inter-enrichment domain continuity is satisfied with high precision. A sufficiently large but finite value is chosen in the numerical simulations for stability and accuracy.

We now turn our attention to the boundary term of the macroscale diffusion problem (Eq. 11). The boundary term is decomposed based on the boundary components analogous to Eq. 18. Along the interface between the enrichment domain and the outer boundaries with Neumann boundary conditions:

$$\left(v^M, q_\alpha^m\right)_{\Gamma_\alpha^q}^c = \left(v^M, \tilde{q}_\alpha\right)_{\Gamma_\alpha^q}^c \quad (27)$$

Along the inter-enrichment domain boundaries and the boundary region - substrate region

interface, using the general form of the boundary constraint yields:

$$\left(v^M, q_\alpha^m\right)_{\Gamma_\alpha^{\text{int}}}^c = -\sum_{\beta \in I_\alpha} \kappa \left(v^M, c_\alpha^m\right)_{\Gamma_\alpha^\beta}^c \tag{28}$$

$$\left(v^M, q_\alpha^m\right)_{\Gamma_\alpha^s}^c = -\kappa \left(v^M, c_\alpha^m\right)_{\Gamma_\alpha^s}^c \tag{29}$$

The inter-enrichment continuity constraint ensures that the microscale flux terms (Eq. 28) across the enrichment domain boundaries cancel for each master-slave pair. Substituting Eqs. 27 and 29 into Eq. 11, leads to the following weak form of the macroscale diffusion problem:

$$a\left(v^M, c^M\right)_\Omega^c + \left(v^M, \dot{c}^M\right)_\Omega^c = \left(v^M, \tilde{q}^M\right)_{\Gamma^q}^c + \sum_{\alpha=1}^{n_{\text{en}}} \left[\left(v^M, \tilde{q}_\alpha\right)_{\Gamma_\alpha^q}^c - \kappa \left(v^M, c_\alpha^m\right)_{\Gamma_\alpha^s}^c - a\left(v^M, c_\alpha^m\right)_{\Omega_\alpha}^c - \left(v^M, \dot{c}_\alpha^m\right)_{\Omega_\alpha}^c\right] \tag{30}$$

2.2 Deformation problem

In this section, we formulate the VME method with the mixed boundary conditions for deformation problems. The equilibrium equation is expressed as:

$$\nabla \cdot (\mathbf{L}(\mathbf{x}) : \nabla \mathbf{u}(\mathbf{x})) = \mathbf{0}; \quad \mathbf{x} \in \Omega \tag{31}$$

where, $\mathbf{u}$ is the displacement vector; $\mathbf{L} \in L^\infty(\Omega)^{n_{sd} \times n_{sd} \times n_{sd} \times n_{sd}}$ the fourth order tensor of elastic moduli taken to be symmetric, elliptic and bounded:

$$L_{ijkl} = L_{klij} = L_{jikl} = L_{ijlk} \tag{32}$$

$$\exists \lambda, \Lambda > 0 \;\text{ such that }\; \lambda \|\boldsymbol{\zeta}\| \leq \boldsymbol{\zeta} : \mathbf{L} : \boldsymbol{\zeta} \leq \Lambda \|\boldsymbol{\zeta}\| \quad \forall \boldsymbol{\zeta} \in \mathbb{R}^{n_{sd} \times n_{sd}} \tag{33}$$

Similar to the diffusivity, the elastic moduli oscillate spatially within the boundary region due to the microstructural heterogeneity. The boundary conditions of the deformation problem is given as:

Displacement B.C.: $$\mathbf{u}(\mathbf{x}) = \tilde{\mathbf{u}}(\mathbf{x}); \quad \mathbf{x} \in \Gamma^u \tag{34}$$

Traction B.C.: $$\boldsymbol{\sigma}(\mathbf{x}) \cdot \mathbf{n} = \tilde{\mathbf{t}}(\mathbf{x}); \quad \mathbf{x} \in \Gamma^t \tag{35}$$

where, $\tilde{\mathbf{u}}$ and $\tilde{\mathbf{t}}$ are prescribed displacement and traction data along the essential ($\Gamma^e = \Gamma^u$ and natural ($\Gamma^n = \Gamma^t$) boundaries, respectively (such that $\Gamma = \Gamma^u \cup \Gamma^t$; $\Gamma^u \cap \Gamma^t \equiv \emptyset$); $\boldsymbol{\sigma} = \mathbf{L} : \nabla \mathbf{u}$ the stress tensor; and : denotes double inner product.

The displacement field is decomposed into the macroscale and microscale components using

the additive split:

$$\mathbf{u}(\mathbf{x}) = \mathbf{u}^M(\mathbf{x}) + \sum_{\alpha=1}^{n_{\text{en}}} \mathcal{H}(\Omega_\alpha)\, \mathbf{u}_\alpha^m(\mathbf{x}) \tag{36}$$

in which, $\mathbf{u}^M$ and $\mathbf{u}_\alpha^m$ are the macroscale approximation to the displacement field and the microscale correction within the enrichment domain, Ω_α, respectively. Introducing the macroscale test function $\mathbf{w}^M \in \mathcal{V}_0^M \subset \left[H_0^1(\Omega)\right]^{n_{sd}}$ and substituting Eq. 36 into Eq. 31, the macroscale deformation equation is expressed in the weak form as:

$$a\left(\mathbf{w}^M, \mathbf{u}^M\right)_\Omega^u = \left(\mathbf{w}^M, \tilde{\mathbf{t}}\right)_{\Gamma^t}^u + \sum_{\alpha=1}^{n_{\text{en}}} \left[\left(\mathbf{w}^M, \mathbf{t}_\alpha^m\right)_{\Gamma_\alpha \setminus \Gamma}^u - a\left(\mathbf{w}^M, \mathbf{u}_\alpha^m\right)_{\Omega_\alpha}^u\right] \tag{37}$$

$\mathbf{t}_\alpha^m = \mathbf{L} : \nabla \mathbf{u}_\alpha^m \cdot \mathbf{n}$ is the microscale tractions along the boundary of the enrichment domain. The bilinear form and the L_2 inner product for the deformation problem are, respectively:

$$a(\mathbf{u}, \mathbf{w})_{[\cdot]}^u \equiv \int_{[\cdot]} \nabla \mathbf{u} : \mathbf{L} : \nabla \mathbf{w}\, d[\cdot] \tag{38}$$

$$(\mathbf{u}, \mathbf{w})_{[\cdot]}^u \equiv \int_{[\cdot]} \mathbf{u} \cdot\, \mathbf{w}\, d[\cdot] \tag{39}$$

The solution of the macroscale problem is sought within the solution space $\mathcal{V}_{\tilde{\mathbf{u}}^M}^M(\Omega) \subset \left[H_{\tilde{\mathbf{u}}^M}^1(\Omega)\right]^{n_{sd}}$; and $\tilde{\mathbf{u}}^M$ is the approximation of the boundary displacement data using the macroscale basis functions.

Considering the microscale solution, $\mathbf{u}_\alpha^m \in \mathcal{V}_{\alpha,\tilde{\mathbf{u}}_\alpha}(\Omega_\alpha) \subset \left[H_{\tilde{\mathbf{u}}_\alpha}^1(\Omega_\alpha)\right]^{n_{sd}}$, the weak form of the microscale deformation problem is obtained as:

$$a(\mathbf{w}_\alpha^m, \mathbf{u}_\alpha^m)_{\Omega_\alpha}^u = \left(\mathbf{w}_\alpha^m, \mathbf{t}^M\right)_{\Gamma_\alpha \setminus \Gamma_\alpha^u}^u + (\mathbf{w}_\alpha^m, \mathbf{t}_\alpha^m)_{\Gamma_\alpha \setminus \Gamma_\alpha^u}^u - a\left(\mathbf{w}_\alpha^m, \mathbf{u}^M\right)_{\Omega_\alpha}^u \tag{40}$$

for every $\mathbf{w}_\alpha^m \in \mathcal{V}_{\alpha,0}(\Omega_\alpha)$.

We propose the following family of boundary conditions along the microscale boundaries for the deformation problem:

$$\theta\left(\mathbf{u}_\alpha^m - \hat{\mathbf{u}}_\alpha\right) + (1-\theta)^\gamma \left(\mathbf{t}_\alpha^m - \hat{\mathbf{t}}_\alpha\right) = 0; \quad \mathbf{x} \in \Gamma_\alpha \tag{41}$$

This boundary conditions is analogous to the one proposed for the diffusion problem and is rewritten in terms of a single parameter, κ, as:

$$\mathbf{t}_\alpha^m = \hat{\mathbf{t}}_\alpha - \kappa\left(\mathbf{u}_\alpha^m - \hat{\mathbf{u}}_\alpha\right) \tag{42}$$

The arguments made in the derivation of the boundary terms for the diffusion problem can be applied without difficulty to the deformation problem. It is trivial to show that the weak

form of the macroscale deformation problem is expressed as:

$$a\left(\mathbf{w}^M,\mathbf{u}^M\right)_\Omega^u=\left(\mathbf{w}^M,\tilde{\mathbf{t}}^M\right)_{\Gamma^t}^u+\sum_{\alpha=1}^{n_{\text{en}}}\left[\left(\mathbf{w}^M,\tilde{\mathbf{t}}_\alpha\right)_{\Gamma_\alpha^t}^u-\kappa\left(\mathbf{w}^M,\mathbf{u}_\alpha^m\right)_{\Gamma_\alpha^s}^u-a\left(\mathbf{w}^M,\mathbf{u}_\alpha^m\right)_{\Omega_\alpha}^u\right] \tag{43}$$

where, $\tilde{\mathbf{t}}^M$ is the approximation to the prescribed boundary traction using a coarse grid, and $\tilde{\mathbf{t}}_\alpha$ the microscale correction to the prescribed boundary traction. The weak form of the microscale deformation problem at the enrichment domain, Ω_α, yields:

$$\begin{aligned}a\left(\mathbf{w}_\alpha^m,\mathbf{u}_\alpha^m\right)_{\Omega_\alpha}^u&=\left(\mathbf{w}_\alpha^m,\tilde{\mathbf{t}}_\alpha\right)_{\Gamma_\alpha^t}^u+\left(\mathbf{w}_\alpha^m,\mathbf{t}^M\right)_{\Gamma_\alpha}^u\\&-\kappa\left(\mathbf{w}_\alpha^m,\mathbf{u}_\alpha^m\right)_{\Gamma_\alpha^s}^u-\sum_{\beta\in I_\alpha^m}\kappa\left(\mathbf{w}_\alpha^m,\mathbf{u}_\alpha^m\right)_{\Gamma_\alpha^\beta}^u-\sum_{\beta\in I_\alpha^s}\kappa_\infty\left(\mathbf{w}_\alpha^m,\mathbf{u}_\alpha^m-\mathbf{u}_\beta^m\right)_{\Gamma_\alpha^\beta}^c-a\left(\mathbf{w}_\alpha^m,\mathbf{u}^M\right)_{\Omega_\alpha}^u\end{aligned} \tag{44}$$

3 Computational Implementation

In this section, finite element formulation of the micro- and macroscale diffusion and deformation problems is presented and the implementation strategy to evaluate the coupled multiscale problems is discussed.

3.1 Finite element discretization

The macroscale and microscale concentration fields are discretized by setting the pertinent solution spaces as:

$$\mathcal{W}_{\tilde{c}^M}^M\left(\Omega\right)=\left\{c^M\left(\mathbf{x},t\right)\;\middle|\;c^M\left(\mathbf{x},t\right)=\sum_{A=1}^{M}N_A(\mathbf{x})\hat{C}_A(t);\;\hat{C}_A(t)=\tilde{c}\left(\mathbf{x}_A,t\right)\;\text{if }\mathbf{x}_A\in\Gamma^c\right\} \tag{45}$$

$$\mathcal{W}_{\alpha,0}\left(\Omega_\alpha\right)=\left\{c_\alpha^m\;\middle|\;c_\alpha^m\left(\mathbf{x},t\right)=\sum_{a=1}^{m_\alpha}n_{\alpha,a}(\mathbf{x})\hat{c}_{\alpha,a}(t);\;\hat{c}_{\alpha,a}(t)=0\text{ if }\mathbf{x}_a\in\Gamma_\alpha^c\right\} \tag{46}$$

in which, M and m_α denote the number of nodes in the macroscale mesh discretizing Ω, and the microscale mesh discretizing Ω_α, respectively; N_A and $n_{\alpha,a}$ are the shape functions for the macro- and microscale fields, respectively; $\hat{C}_A$ and $\hat{c}_{\alpha,a}$ are macro- and microscale nodal concentration coefficients; and $\mathbf{x}_A$ and $\mathbf{x}_a$ denote nodal coordinates. In the present formulation, the macro- and microscale grids are taken to be nested such that one macroscale finite element coincides with one enrichment domain within the boundary region. Formulation based on arbitrary positioning of microscale grids may present additional challenges to the computational implementation of the method, such as the treatment of microscale domain vertices and enforcement of rigid body constraints. Following the standard Bubnov-Galerkin setting, the corresponding test functions for the macro- and microscale problems are discretized using the same shape functions. In the present formulation, we also make the simplifying (but not a necessary) assumption that the boundary data is smooth and does not have microscale

components. We further consider a set of discrete time points $\tilde{\mathcal{T}} = \{t_i \,|\, t_i \in \mathcal{T};\, t_{i+1} > t_i\}$ within the observation period, $\mathcal{T}$ and set $\Delta t = t_{i+1} - t_i$. Substituting Eq. 45 into Eq. 30 and employing a backward difference approximation to discretize the time derivative yield the following system of equations at the macroscale in the vector form (at time t_{i+1}):

$$\boldsymbol{\Psi} := \left(\mathbf{M}^c + \Delta t \mathbf{K}^c\right) \hat{\mathbf{C}} - \mathbf{M}^c \, {}_{t_i}\hat{\mathbf{C}} - \mathbf{f}^c = \mathbf{0} \tag{47}$$

where, $\hat{\mathbf{C}} = \{\hat{C}_1, \hat{C}_2, \ldots, \hat{C}_M\}^T$ denotes the vector of macroscale nodal concentration coefficients; the left subscript ${}_{t_i}(\cdot)$ denotes the value at the previous time step; and

$$\mathbf{M}^c = \underset{A,B}{\mathbf{A}} \left(N_A, N_B\right)^c_\Omega ; \quad \mathbf{K}^c = \underset{A,B}{\mathbf{A}} \, a\left(N_A, N_B\right)^c_\Omega \tag{48}$$

$$\begin{aligned} \mathbf{f}^c = \underset{A}{\mathbf{A}} \Bigg\{ \left(N_A, \tilde{q}^M\right)^c_{\Gamma^q} + \sum_{\alpha=1}^{n_{\text{en}}} \sum_{a=1}^{m_\alpha} \Big[& \Delta t \, \kappa \left(N_A, n_{\alpha,a}\right)^c_{\Gamma^s_\alpha} \hat{c}_{\alpha,a} \\ & - \Delta t \, a\left(N_A, n_{\alpha,a}\right)^c_{\Omega_\alpha} \hat{c}_{\alpha,a} - \left(N_A, n_{\alpha,a}\right)^c_{\Omega_\alpha} \Delta \hat{c}_{\alpha,a} \Big] \Bigg\} \end{aligned} \tag{49}$$

in which, $\mathbf{A}$ denotes standard finite element assembly operation, and $\Delta(\cdot) = (\cdot) - {}_{t_i}(\cdot)$.

Remark 2. *In the construction of $\mathbf{K}^c$, it is necessary to evaluate the integration of the bilinear form on the boundary and substrate regions separately. Within the boundary region, the diffusivity of the material oscillates spatially, whereas the substrate domain is characterized by a homogenized diffusivity tensor. The bilinear form of the discretized macroscale problem is expressed as:*

$$a\left(N_A, N_B\right)^c_\Omega = a\left(N_A, N_B\right)^c_{\Omega_s} + \sum_{\alpha=1}^{n_{\text{en}}} a\left(N_A, N_B\right)^c_{\Omega_\alpha} \tag{50}$$

The integration of the bilinear form over the substrate region is standard. We consider the following partitioning of the integral within each enrichment domain:

$$\int_{\Omega_\alpha} \left(\nabla N_A\right)^T \mathbf{D} \left(\nabla N_B\right) d\Omega = \sum_i \int_{e_{\alpha,i}} \left(\nabla N_A\right)^T \mathbf{D} \left(\nabla N_B\right) d\Omega \tag{51}$$

in which, the partitioning coincides with the partitioning of the domain for microscale problems; and $e_{\alpha,i}$ denotes the domain of a microscale finite element; and T is the transpose operator. The integration within $e_{\alpha,i}$ follows the Gaussian quadrature formula with macroscale shape function gradients computed at each integration point of the partition. We note that this is an expensive integration. When the macroscale fields vary smoothly, it is possible to approximate this integral by replacing spatially varying $\mathbf{D}$ by a constant $\bar{\mathbf{D}}$, which is the homogenized diffusivity of the microstructure. This approach leads to the homogenization-like integration scheme [22, 23], which keeps the standard integration of the bilinear form over the entire macroscale domain.

Substituting Eq. 46 into Eqs. 23 and 26, the microscale problems are expressed in the

vector form as (at time t_{i+1}):

$$\boldsymbol{\psi}_\alpha := \left(\mathbf{M}^c_\alpha + \Delta t \mathbf{K}^c_\alpha\right)\hat{\mathbf{c}}_\alpha - \mathbf{M}^c_{\alpha\, t_i}\hat{\mathbf{c}}_\alpha - \mathbf{f}^c_\alpha = \mathbf{0} \tag{52}$$

$\hat{\mathbf{c}}_\alpha = \{\hat{c}_{\alpha,1}, \hat{c}_{\alpha,2}, \ldots, \hat{c}_{\alpha,m_\alpha}\}^T$ denotes the vector of microscale nodal concentration coefficients; and

$$\mathbf{M}^c_\alpha = \underset{a,b}{\mathbf{A}} \left(n_{\alpha,a}, n_{\alpha,b}\right)^c_{\Omega_\alpha} \tag{53}$$

$$\mathbf{K}^c_\alpha = \underset{a,b}{\mathbf{A}} \left[a\left(n_{\alpha,a}, n_{\alpha,b}\right)^c_{\Omega_\alpha} + \kappa\left(n_{\alpha,a}, n_{\alpha,b}\right)^c_{\Gamma^s_\alpha \cup \Gamma^{\beta m}_\alpha} + \kappa_\infty\left(n_{\alpha,a}, n_{\alpha,b}\right)^c_{\Gamma^{\beta s}_\alpha}\right] \tag{54}$$

$$\begin{aligned}\mathbf{f}^c_\alpha = \underset{a}{\mathbf{A}} \Bigg\{ \sum_{A=1}^{M} \Big[&-\Delta t\, a\left(n_{\alpha,a}, N_A\right)^c_{\Omega_\alpha} \hat{C}_A \; - \left(n_{\alpha,a}, N_A\right)^c_{\Omega_\alpha} \Delta \hat{C}_A \Big] \\ &+\kappa_\infty \left(n_{\alpha,a}, c^m_\beta\right)^c_{\Gamma^{\beta s}_\alpha} + \left(n_{\alpha,a}, q^M\right)^c_{\Gamma_\alpha} \Bigg\}\end{aligned} \tag{55}$$

where, $\Gamma^{\beta m}_\alpha = \cup_{\beta \in I^m_\alpha} \Gamma^\beta_\alpha$ and $\Gamma^{\beta s}_\alpha = \cup_{\beta \in I^s_\alpha} \Gamma^\beta_\alpha$.

To discretize the deformation problem, the macro- and microscopic displacement fields are approximated by setting the following solution spaces:

$$\mathcal{V}^M_{\tilde{\mathbf{u}}^M}(\Omega) = \left\{ \mathbf{u}^M(\mathbf{x}) \;\middle|\; \mathbf{u}^M(\mathbf{x}) = \sum_{A=1}^{M} N_A(\mathbf{x}) \hat{\mathbf{U}}_A;\; \hat{\mathbf{U}}_A = \tilde{\mathbf{u}}(\mathbf{x}_A) \text{ if } \mathbf{x}_A \in \Gamma^u \right\} \tag{56}$$

$$\mathcal{V}_{\alpha,0}(\Omega_\alpha) = \left\{ \mathbf{u}^m_\alpha \;\middle|\; \mathbf{u}^m_\alpha(\mathbf{x}) = \sum_{a=1}^{m_\alpha} n_{\alpha,a}(\mathbf{x}) \hat{\mathbf{u}}_{\alpha,a};\; \hat{\mathbf{u}}_{\alpha,a} = 0 \text{ if } \mathbf{x}_a \in \Gamma^u_\alpha \right\} \tag{57}$$

in which, $\hat{\mathbf{U}}_A$ and $\hat{\mathbf{u}}_{\alpha,a}$ are the macro- and microscale nodal displacement coefficients, respectively. Substituting Eqs. 56 and 57 into the macroscale weak form (Eq. 43) yields the discrete macroscale problem:

$$\boldsymbol{\Phi} := \mathbf{K}^u \hat{\mathbf{U}} - \mathbf{f}^u = \mathbf{0} \tag{58}$$

where, $\hat{\mathbf{U}} = \{\hat{\mathbf{U}}^T_1, \hat{\mathbf{U}}^T_2, \ldots, \hat{\mathbf{U}}^T_M\}^T$ denotes the vector of macroscale nodal displacement coefficients; and,

$$\mathbf{K}^u = \underset{A,B}{\mathbf{A}} \, a\left(N_A, N_B\right)^u_\Omega \tag{59}$$

$$\mathbf{f}^u = \underset{A}{\mathbf{A}} \left\{ \left(N_A, \tilde{\mathbf{t}}^M\right)^u_{\Gamma^t} - \sum_{\alpha=1}^{n_{\text{en}}} \sum_{a=1}^{m_\alpha} \left[a\left(N_A, n_{\alpha,a}\right)^u_{\Omega_\alpha} \hat{\mathbf{u}}_{\alpha,a} + \kappa\left(N_A, n_{\alpha,a}\right)^u_{\Gamma^s_\alpha} \hat{\mathbf{u}}_{\alpha,a} \right] \right\} \tag{60}$$

As in the case of the diffusion problem, the tensor of elastic moduli that characterize the behavior within the boundary region oscillates spatially due to the microstructural heterogeneity. The evaluation of the stiffness matrix (Eq. 58) is therefore similar to $\mathbf{K}^c$ as explained

in Remark 2.

The microscale problem in the discrete form is obtained by substituting Eqs. 56 and 57 into the weak form of the microscale problem (Eq. 44):

$$\boldsymbol{\phi}_\alpha := \mathbf{K}^u_\alpha \hat{\mathbf{u}}^\alpha - \mathbf{f}^u_\alpha = \mathbf{0} \tag{61}$$

$\hat{\mathbf{u}}^\alpha = \{(\hat{\mathbf{u}}_{\alpha,1})^T, (\hat{\mathbf{u}}_{\alpha,2})^T, \ldots, (\hat{\mathbf{u}}_{\alpha,m_\alpha})^T\}^T$ is the vector of microscale nodal displacement field coefficients; and,

$$\mathbf{K}^u_\alpha = \underset{a,b}{\mathbf{A}} \left\{ a\left(n_{\alpha,a}, n_{\alpha,b}\right)^u_{\Omega_\alpha} + \kappa\left(n_{\alpha,a}, n_{\alpha,b}\right)^u_{\Gamma^s_\alpha \cup \Gamma^{\beta m}_\alpha} + \kappa_\infty\left(n_{\alpha,a}, n_{\alpha,b}\right)^u_{\Gamma^{\beta s}_\alpha} \right\} \tag{62}$$

$$\mathbf{f}^u_\alpha = \underset{a}{\mathbf{A}} \left\{ \left(n_{\alpha,a}, \mathbf{t}^M\right)^u_{\Gamma_\alpha} + \kappa_\infty\left(n_{\alpha,a}, \mathbf{u}^m_\beta\right)^u_{\Gamma^{\beta s}_\alpha} - \sum_{A=1}^{M} a\left(n_{\alpha,a}, N_A\right)^u_{\Omega_\alpha} \hat{\mathbf{U}}_A \right\} \tag{63}$$

Remark 3. *The solution of the macroscale problem describes the overall (i.e., homogenized) behavior of the system response, whereas the microscale problems describe the enrichment of the response at the boundary region to capture the fluctuations induced by the microstructural heterogeneity. The momentum and mass balance across the macroscale elements, as well as in the microscale problems are satisfied separately in the weak sense as in the standard finite element method. A direct reconstruction of the original response fields would violate the mass and momentum balance across the enrichment domain - substrate interface due to different resolutions of the micro- and macroscale representations. The local mass conservation principle can be enforced by employing a mixed formulation [13].*

Remark 4. *The finite elements employed in the discretization of the macro- and microscale problems must be chosen to ensure linear independence between the pertinent solution spaces as discussed in Remark 1. The standard bilinear (for 2D problems) and trilinear (for 3D problems) Lagrangian shape functions satisfy this condition when the microscale concentration and displacements at the corner nodes of each enrichment domain is set to vanish as in the case of the proposed canopy functions. We note that linear independence is not guaranteed when higher order shape functions are used at both macro- and microscales, but proper choice/design of the appropriate high order of shape functions that satisfy linear independence is possible.*

3.2 Implementation strategy

The VME method with canopy functions has been implemented for two-dimensional diffusion and deformation problems. The implementation strategy of the multiscale approach applied to the diffusion problem is summarized in Box 1. The implementation consists of the initialization and solution phases. The initialization phase consists of setting the initial conditions for the macroscale and each microscale problem, and identification of the boundary components for

each enrichment domain. The initial conditions are set as:

$$\hat{C}_A(0) = c_0(\mathbf{x}_A); \quad A = 1, \ldots, M \tag{64}$$

$$\hat{c}_{\alpha,a}(0) = c_0(\mathbf{x}_a) - \sum_{A=1}^{M} N_A(\mathbf{x}_a)\hat{C}_A(0); \quad a = 1, \ldots, m_\alpha \tag{65}$$

Initialization phase -

1. Set the initial condition for the macroscale problem, $\hat{\mathbf{C}}(0)$.
2. For each microscale problem ($\alpha = 1, \ldots, n_{\text{en}}$):
   (a) Identify the microscale boundary components ($\Gamma_\alpha^{\text{int}}$, Γ_α^s, Γ_α^c and Γ_α^q).
   (b) Set the initial condition for the microscale problem: $\hat{\mathbf{c}}_\alpha(0)$ on Ω_α.

Solution phase -

3. For each time step, $t_i \in \tilde{\mathcal{T}}$

- Loop until convergence
  (a) For each microscale problem ($\alpha = 1, \ldots, n_{\text{en}}$):
      i. Update the microscale problem boundary conditions: $c_\beta^m(\mathbf{x}, t_i)$ on $\Gamma_\alpha^\beta \subset \Gamma_\alpha^{\text{int}}$; $\hat{q}_\alpha(\mathbf{x}, t_i)$ on Γ_α^q
      ii. Solve the microscale problem, $c_\alpha^m(\mathbf{x}, t_i)$ on Ω_α.
  (b) Solve the macroscale problem, $c^M(\mathbf{x}, t_i)$ on Ω.
  (c) Convergence: $\|c^M - c^M_{\text{prev}}\|/\|c^M\| \leq$ tolerance $\rightarrow$ Exit loop.
  (d) No convergence: $\|c^M - c^M_{\text{prev}}\|/\|c^M\| >$ tolerance $\rightarrow c^M_{\text{prev}} = c^M$

Box 1: Implementation strategy for the multiscale approach applied to the diffusion problem.

We consider a coarse finite element discretization of the macroscale problem domain using bilinear quadrilateral Lagrangian elements. The skeleton of the macroscale discretization within the boundary region is denoted as:

$$\mathcal{S}_b^M = \bigcup_{\alpha=1}^{n_{\text{en}}} \bigcup_{s=1}^{n_{\text{edge}}} \gamma_{\alpha,s}^M \tag{66}$$

where, $\gamma_{\alpha,s}^M \subset \partial\Omega_\alpha$ denotes an element edge; and n_{edge} the total number of edges of a single macroscale element. Considering a discretization of the microscale problem using bilinear quadrilateral Lagrangian elements, the part of the skeleton that lies along the boundary of the microscale domain is denoted as: $\mathcal{S}_{\alpha,s}^m = \cup_{i=1}^{m_{\alpha,s}} \gamma_{\alpha,s,i}^m$, where $\gamma_{\alpha,s,i}^m$ is a microscale element edge and $m_{\alpha,s}$ the total number of microscale element edges that lie on $\gamma_{\alpha,s}^M$. The microscale boundary components are identified by determining whether $\gamma_{\alpha,s}^M$ lies on the natural boundary condition (Γ^n), essential boundary condition (Γ^e) or the substrate boundary (Γ_α^s). Microscale

boundary edges, $\gamma^m_{\alpha,s,i}$ are assigned as Γ^n_α, Γ^e_α or Γ^s_α accordingly. If $\gamma^M_{\alpha,s}$ is an inter-enrichment domain boundary (i.e., $\exists\beta$ such that $\gamma^M_{\alpha,s} = \gamma^M_{\beta,p}$), all $\gamma^m_{\alpha,s,i}$ are assigned as master (if $\beta < \alpha$) or a slave (if $\beta > \alpha$) enrichment domain boundary.

Remark 5. *It is clear that the numbering of the enrichment domains influence the choice of enrichment domain boundary master-slave pairs in the implementation of the proposed algorithm. This bears resemblance to the domain decomposition approach based on the multiplicative Schwartz method, where the coupling between the problem subdomains is affected by the subdomain ordering. Similar to the multiplicative Schwartz method [24], numerical experiments indicated that the choice of enrichment domain numbering does not significantly affect the accuracy and convergence characteristics of the method.*

At each time increment, the multiscale problem is evaluated iteratively. Within an iteration loop, each microscale problem is evaluated by solving Eq. 52. The microscale boundary conditions are updated prior to solving each microscale problem. Each slave enrichment domain boundary requires the response field computed at the enrichment domain that holds the corresponding master domain boundary. Owing to the master-slave pairing strategy described above, the response fields for the master domain boundaries are always computed prior to the corresponding slave boundaries. In the current (serial) implementation, this approach leads to near identical computational efficiency of the proposed mixed boundary conditions compared to imposing homogeneous boundary conditions. In contrast, parallel implementation of the VME method with mixed boundary conditions is more complex than with homogeneous boundary conditions since information from master domain boundaries needs to be communicated (possibly across processors) to the enrichment domains. Since the microscale problem at each enrichment domain is evaluated independent of the problems at the neighboring enrichment domains, enforcement of continuity does not necessarily imply imposing nodal compatibility across the neighboring enrichment domains. The inter-enrichment domain continuity may be implemented strongly (i.e., along every point of the discretized boundary domains) or weakly (i.e., only at nodal positions). In the strong implementation, nodal compatibility is typically unavoidable. In the weak implementation - more suitable for non-periodic microstructures - the nodal values of the slave boundary response are approximated from the master boundary response. The macroscale problem is evaluated using Eq. 47 along with the solution of all microscale problems at the current iteration. The convergence of the solution is checked based on the macroscale solution using the energy norm as shown in Box 1. We note that in all numerical examples investigated, the microscale response fields at each enrichment domain also converged up to the tolerance value. When large time step sizes are considered, the convergence of the microscale problems may become critical for solution accuracy. This issue can be alleviated by checking the solution convergence based on both microscale and macroscale solutions, and by considering separate time step sizes for the micro- and macroscale problems. It is straightforward to extend the proposed algorithm to include multiple convergence criterion and separate time step sizes for the macroscale and the microscale problems. Box 2

illustrates the implementation strategy for the deformation problem. The proposed strategy for the deformation problem follows closely with the strategy for the diffusion problem.

Initialization phase -

1. For each microscale problem ($\alpha = 1, \ldots, n_{\text{en}}$):
   - Identify the microscale boundary components ($\Gamma_\alpha^{\text{int}}$, Γ_α^s, Γ_α^u and Γ_α^t).

Solution phase -

2. Loop until convergence
   (a) For each microscale problem ($\alpha = 1, \ldots, n_{\text{en}}$):
      i. Update the microscale problem boundary conditions: $\mathbf{u}_\beta^m(\mathbf{x})$ on $\Gamma_\alpha^\beta \subset \Gamma_\alpha^{\text{int}}$; $\hat{\mathbf{t}}_\alpha(\mathbf{x})$ on Γ_α^t
      ii. Solve the microscale problem, $\mathbf{u}_\alpha^m(\mathbf{x})$ on Ω_α.
   (b) Solve the macroscale problem, $\mathbf{u}^M(\mathbf{x})$ on Ω.
   (c) Convergence: $\|\mathbf{u}^M - \mathbf{u}_{\text{prev}}^M\|/\|\mathbf{u}^M\| \leq$ tolerance $\rightarrow$ Exit loop.
   (d) No convergence: $\|\mathbf{u}^M - \mathbf{u}_{\text{prev}}^M\|/\|\mathbf{u}^M\| >$ tolerance $\rightarrow \mathbf{u}_{\text{prev}}^M = \mathbf{u}^M$

Box 2: Implementation strategy for the multiscale approach applied to the deformation problem.

The solution algorithms for the diffusion and deformation problems are implemented using the commercial software program, Diffpack, which is an object oriented development framework for numerical solution of partial differential equations [25]. DiffPack provides a library of $C++$ classes to facilitate development of solution algorithms for complex PDEs. When coupled diffusion-elasticity problems are considered, such as when the elastic moduli is a function of concentration and when the diffusivity is a function of elastic moduli, it is possible to evaluate the diffusion and deformation problems in a coupled manner. Such a coupled solution algorithm based on the operator split method has been proposed and detailed in Ref. [10] for the VME method with RFB functions. The extension of this methodology to the VME method with canopy functions is straightforward and does not require special treatment of the multiphysics coupling.

4 Numerical Verification

4.1 Nonuniform diffusion into biphasic boundary region

We consider a 2.5 mm $\times$ 2.5 mm specimen with geometry and boundary conditions illustrated in Fig. 3. The boundary region constitutes the top 1 mm of the specimen and consists of two phases illustrated as dark (phase a) and light (phase b) colors. A nonuniform prescribed boundary concentration is applied to create a two-dimensional diffusion within the numerical specimen. The magnitude of the prescribed boundary concentration is 5%. The initial

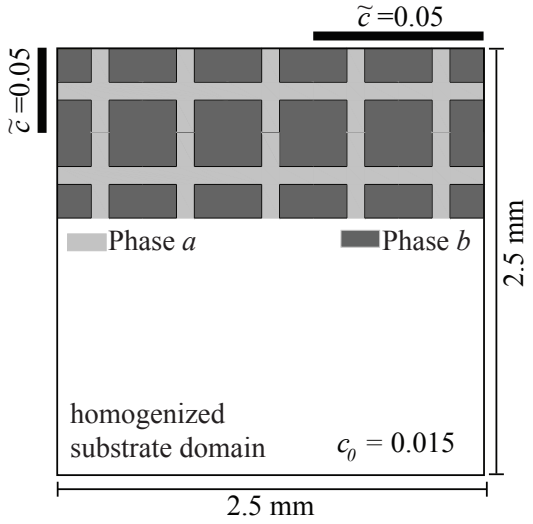

Figure 3: Geometry and boundary conditions of the plane strain panel.

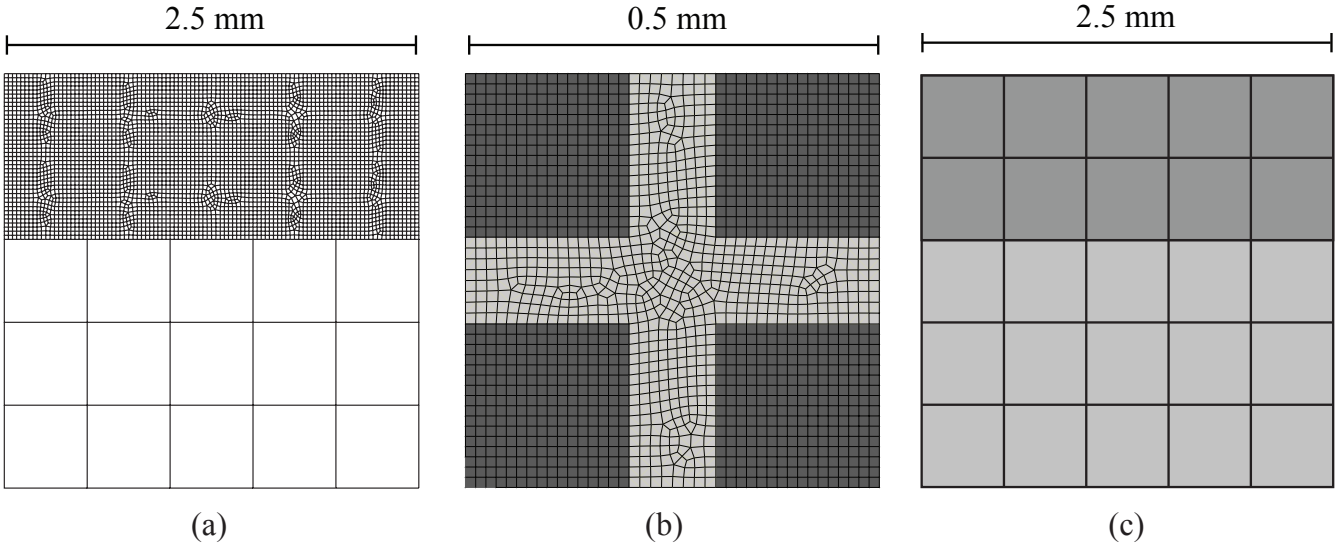

Figure 4: (a) Discretization of the reference finite element model; (b) Microscale discretization of an enrichment domain; and, (c) macroscale discretization of the numerical specimen with enriched (darker) elements.

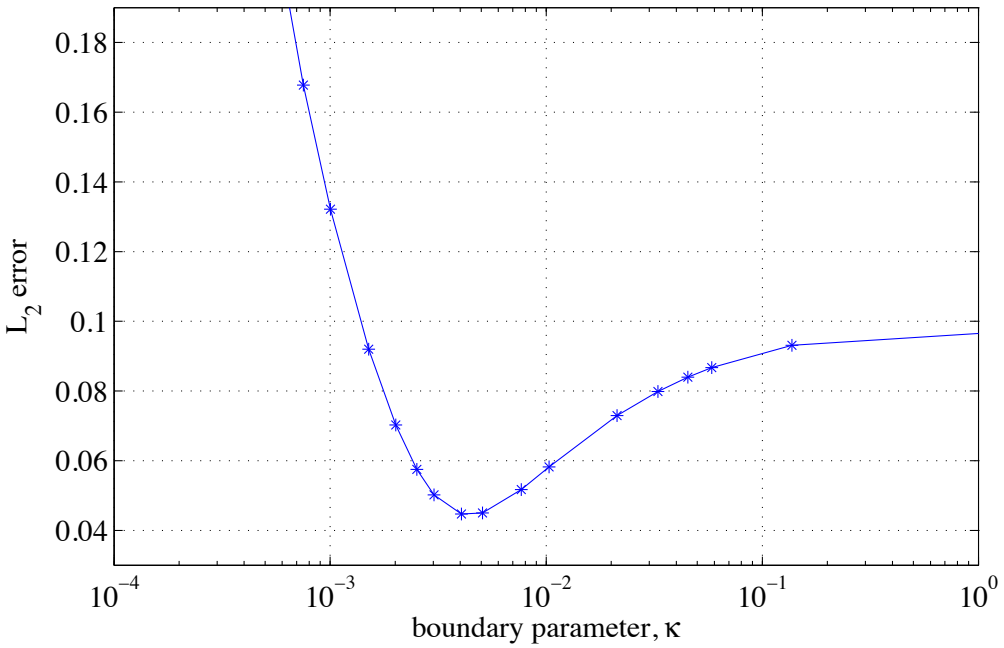

Figure 5: The effect of boundary parameter, κ on modeling error in diffusion simulations.

concentration within the problem domain is 1.5%. The performance of the proposed multiscale approach is verified against direct numerical simulations. In the reference model, the microstructure within the boundary region is fully resolved (Fig. 4a), whereas the substrate region discretization remains coarse. The field continuity along the nonconforming substrate-boundary region interface is enforced using the penalty formulation [26]. The micro- and macroscale discretizations of the multiscale model are illustrated in Fig. 4b and Fig. 4c, respectively. The microscale mesh has the same mesh density as the mesh employed in the discretization of the boundary region of the reference model.

In the first set of simulations, we illustrate the effect of the microscale boundary condition on the accuracy characteristics of the proposed multiscale approach. The apparent diffusivity contrast between the two phases is $D^a/D^b = 50$. These simulations are conducted for the duration of 125 hours, with time step size of 50 minutes for both the VME and reference model. The time step sizes are small enough such that further refinement of the time step does not significantly affect the solution accuracy. Figure 5 illustrates the effect of the boundary parameter, κ, on the accuracy of the VME approach. In all simulations, the boundary parameter, γ, is set to 3.0. The value set for γ has insignificant influence on the accuracy of the proposed approach, and the chosen parameter value ensures that a small variation in θ leads to a relatively large change in κ permitting a convenient probing of the microscale boundary conditions, particularly around the homogeneous boundary condition limit. The modeling errors are minimized when the boundary parameter, κ is approximately 4e-3. Compared to the homogeneous boundary conditions (i.e., using RFB functions), the proposed boundary condition (i.e., using canopy functions) with the optimal boundary parameter value is significantly more

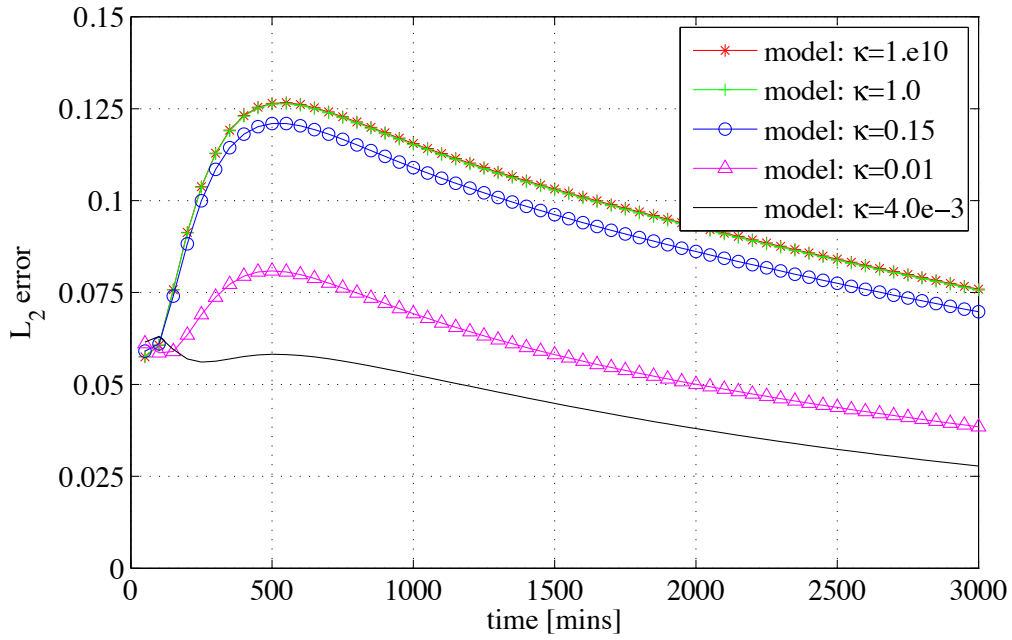

Figure 6: Model error as a function of simulation time.

accurate (i.e., 9.5% using the RFB functions compared to 4.5% with the canopy functions) in these simulations. The accuracy of the predictions degrades as the boundary parameter approaches the flux free as well as the homogeneous boundary condition limits. The rate of degradation is significantly higher as the boundary condition approaches the flux free case ($\theta \to 0$), whereas the errors converge to a higher yet stable value when ($\theta \to 1$). The L_2 error presented in Fig. 5 is time averaged over the duration of the simulation. The evolution of the L_2 error as a function of time is shown in Fig. 6 for a range of boundary parameter values. While the homogeneous boundary conditions are reasonably accurate at the steady state of the diffusion response, modeling errors tends to be higher at the transient regime. The accuracy of the proposed boundary condition also increases in time. The error characteristics within the transient regime is not sensitive to the boundary parameter value when (approximately $0.3 \leq \theta < 1.0$ or $1 \leq \kappa < \infty$). The error within the transient regime reduces as the boundary parameter approaches the optimal value. The increase in model error at the transient regime is not pronounced when the proposed boundary condition is employed.

Figures 7 and 8 show the concentration profiles computed using direct numerical simulations and the concentration response computed using the multiscale model. The concentration profile in the multiscale model is computed by adding the macro- and the pertinent microscale response fields at the enriched domains. Figure 7 shows the concentration profiles along a vertical cross-section 2 mm from the left of the specimen for two time instants within the transient regime. In both time instances, the predictions with the proposed boundary condition (with κ=4.0e-3) are more accurate than those obtained using the homogeneous boundary conditions as well as when the boundary parameter approaches the flux free limit. Figure 8

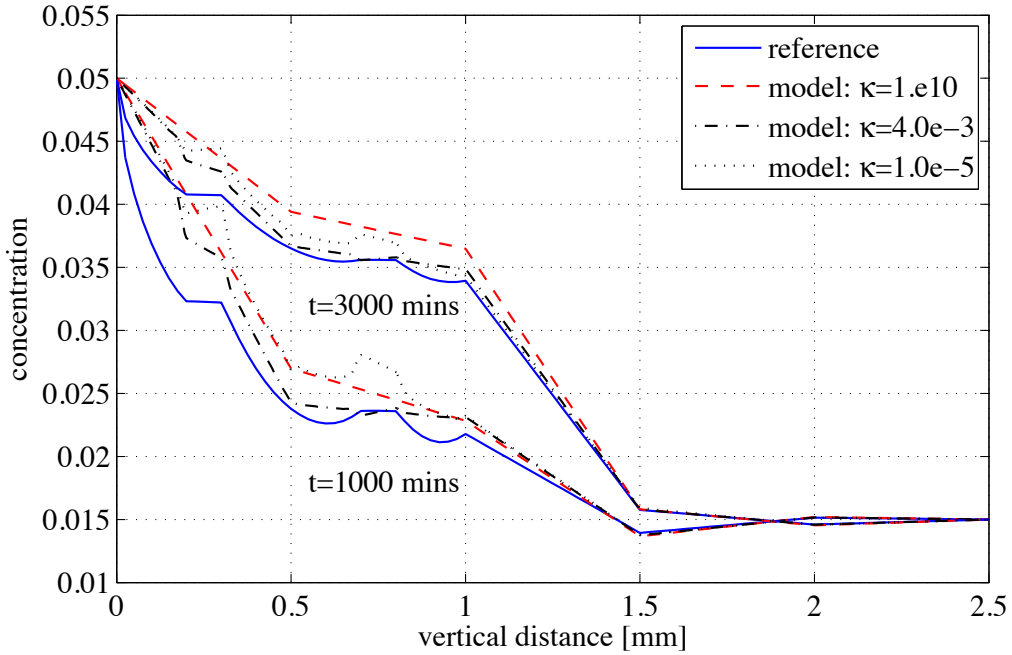

Figure 7: Concentration profiles computed based on the VME and the reference model at a vertical cross-section at the middle of the numerical specimen.

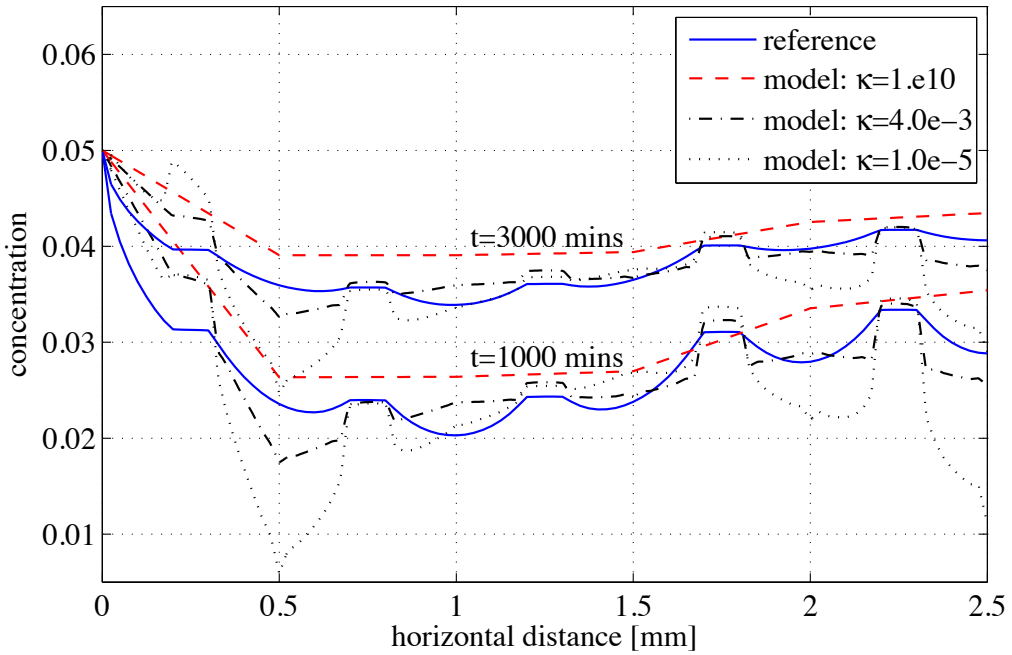

Figure 8: Concentration profiles computed based on the VME and the reference model at an horizontal cross-section 1 mm below the top of the numerical specimen.

Table 1: Optimal boundary condition parameter for a range of diffusivity contrasts.

D^a/D^b	1/50	1/25	1/5	1	5	25	50
κ	3.0e-3	7.5e-3	4.0e-3	2.0e-3	1.5e-3	3.0e-3	4.0e-3

shows the concentration profiles from a horizontal cross-section, 0.5 mm from the top of the specimen. The response computed using the VME approach closely approximates the overall behavior within the boundary region, with better accuracy with the proposed boundary conditions. In Figs. 7 and 8 the cross sections coincide with the internal boundaries of the enrichment domains. Since the microscale response vanishes at the internal boundaries when homogeneous boundary condition is imposed (i.e., $\kappa = 1e10$), the full multiscale response is equal to its macroscale counterpart. When the boundary parameter approaches the flux free limit ($\kappa \to 0$), we observed formation of fluctuations in the concentration response in the vicinity of the applied concentration boundary. These fluctuations appear to be due to the discretization errors associated with the transient diffusion process. This indicates that when the microscale boundary condition approaches the flux free limit, the effect of the microscale solution on the macroscopic response is reduced and the microscale solution fails to regularize the macroscale response.

We then conducted a series of simulations to study the sensitivity of the optimal boundary condition parameter, κ, to the material parameters within the microstructure. Table 1 summarizes the values of the optimal boundary condition parameter as a function of the diffusivity contrast. The boundary condition appears to change values as a function of the diffusivity contrast, but remains within a reasonably narrow range for a wide spectrum of diffusivity contrasts. κ =4.0e-3 yielded better accuracy than the homogeneous boundary condition for all cases considered in this study. The microstructure employed in this study leads to non-uniform and two dimensional transport conditions to better assess the sensitivity of the model to the variations in the boundary parameter, κ. Concentration fluxes across the microstructures, particularly at the beginning of the simulations are relatively high. The results of the sensitivity study therefore points to the relative insensitivity of the optimal boundary parameter with respect to the high flux and multi-dimensional transport conditions, in addition to the diffusivity contrast. Physically, the low (i.e., 4e-3) value of κ indicates that the variation of the concentration across microstructure boundaries is non-uniform.

4.2 Elastic response of inclusion reinforced composites

The performance of the multiscale model is also assessed in the setting of elliptic (i.e., elasticity) problems. The geometries and the boundary conditions for the problems considered are illustrated in Fig. 9. The first problem is the uniaxial tensile response of a periodic composite with uniform circular inclusions, whereas the second problem is defined on a periodic composite with three inclusions with different sizes subjected to uniaxial tension. The response computed based on the VME method with the canopy functions is compared to the

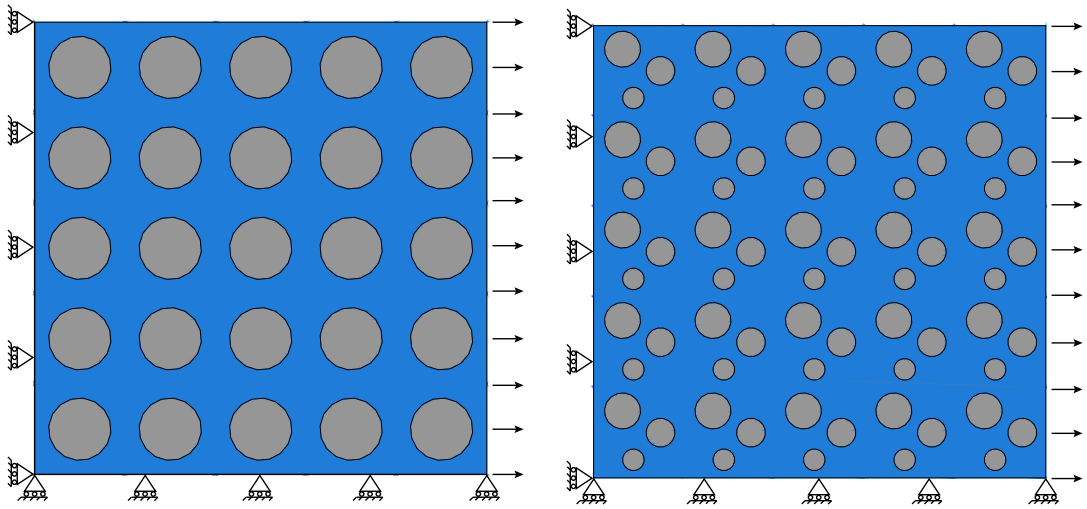

Figure 9: The geometry and boundary conditions of (a) one inclusion model; and, (b) three inclusions model.

direct numerical simulations (i.e., the finite element method) with full discretization of the problem domains (Fig. 9). In the VME simulations, the macroscale grid is a uniform grid with 25 quadrilateral elements. The microscale grids considered for the single inclusion and three-inclusion problems are shown in Fig. 10.

First, we investigate the effect of the boundary parameter on the solution accuracy in the context of the single inclusion problem. Two microstructure parameters characterize the composite: (1) the stiffness contrast, $r = E_i/E_m$ with E_i and E_m denoting the elastic moduli of the inclusion and matrix, respectively; (2) inclusion volume fraction, $\nu = V_i/V$ with V_i and V are the volume of the inclusion phase and the total volume of the microstructure, respectively. The composite material is subjected to macroscopic tensile stress as illustrated in Fig. 9. The Poisson's ratio of the inclusion and matrix are taken to be the same. The boundary exponent parameter, γ is set as 3.0. Figure 11 illustrates the L_2 error of the proposed multiscale approach compared to the direct numerical simulation as a function of the boundary parameter, θ for various values of the constituent stiffness contrast (1e-3 $\leq r \leq$ 10) and the inclusion volume fraction ($15\% \leq \nu \leq 67.5\%$). In contrast to the parabolic (i.e., diffusion) problem, the optimal value of the boundary parameter is close to the homogeneous boundary condition $\theta = 1$ in the present case. The VME error typically dips to an optimal boundary parameter value, θ_{opt} and increases rapidly as θ is further reduced. Relaxation of the boundary parameter has a much more pronounced effect on the solution accuracy for high volume fraction and high stiffness contrast values. For instance, the VME error reduces from 8% to less than 2% for the microstructure with $\nu = 67.5\%$ and $r = 0.1$. For lower volume fraction materials and low stiffness contrasts, there is no clear optimal boundary parameter different from the RFB limit ($\theta = 1$). This is because at small inclusion volume fractions, the heterogeneity of the

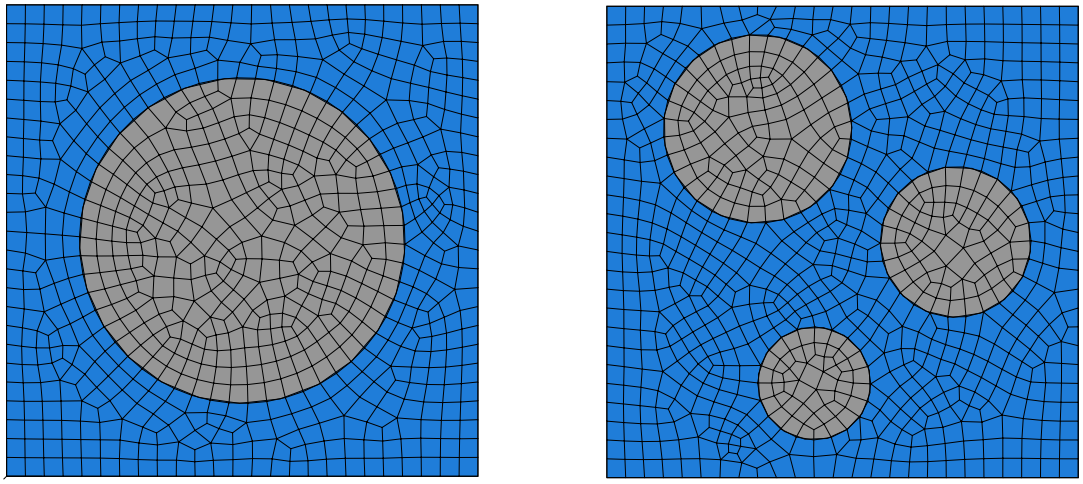

(a) (b)

Figure 10: The geometry and discretization of the microstructure meshes for (a) one inclusion model; and, (b) three inclusions model.

Table 2: Coefficients of the optimal boundary parameter model.

When $r > 1$:	$n = 2$	m=5			
p_{00}=9.997e-1	p_{01}=-7.445e-4	p_{02}=-7.227e-2	p_{03}=2.992e-1	p_{04}=-4.436e-1	p_{05}=2.251e-1
p_{10}=-6.624e-4	p_{11}=-2.472e-3	p_{12}=4.821e-3	p_{13}=-1.341e-3	p_{14}=-2.882e-3	p_{15}=0
p_{20}=3.363e-5	p_{21}=7.925e-6	p_{22}=-1.625e-4	p_{23}=2.898e-4	p_{24}=0	p_{25}=0
When $r < 1$:	$n = 3$	m=4			
p_{00}=1.0	p_{01}=-5.241e-2	p_{02}=1.097e-1	p_{03}=-1.588e-2	p_{04}=-1.735e-1	
p_{10}=-4.298e-3	p_{11}=3.094e-2	p_{12}=-1.244e-1	p_{13}=6.975e-1	p_{14}= 0	
p_{20}=1.858e-1	p_{21}=-2.986e-1	p_{22}=-1.313	p_{23}=0	p_{24}=0	
p_{30}=-4.727e-1	p_{31}=1.835	p_{32}= 0	p_{33}=0	p_{34}=0	

deformation field is localized within the enriched element (through St. Venant's principle) and the boundaries of the domain has less influence on the microscale response.

Figure 12 illustrates the variation of the optimal boundary parameter as a function of the microstructural characteristics. The figure indicates that the optimal boundary parameter varies within a narrow range of values (between 0.96 and 1.0) and is influenced by the microstructure characteristics. A single value of θ_{opt} cannot be identified in view of the sensitivity of the model error (Fig. 11) to the boundary parameter. Alternatively, we consider a polynomial fit for the optimal boundary parameter as a function of the microstructure parameters, r and ν:

$$\tilde{\theta}_{\text{opt}}(r,\nu) = \sum_{a=0}^{n}\sum_{b=0}^{m} p_{ab} r^a \nu^b \tag{67}$$

Figure 13 shows the fitted optimal boundary parameter function. The parameters of the function are provided in Table 2.

The performance of the proposed optimal boundary parameter function is demonstrated

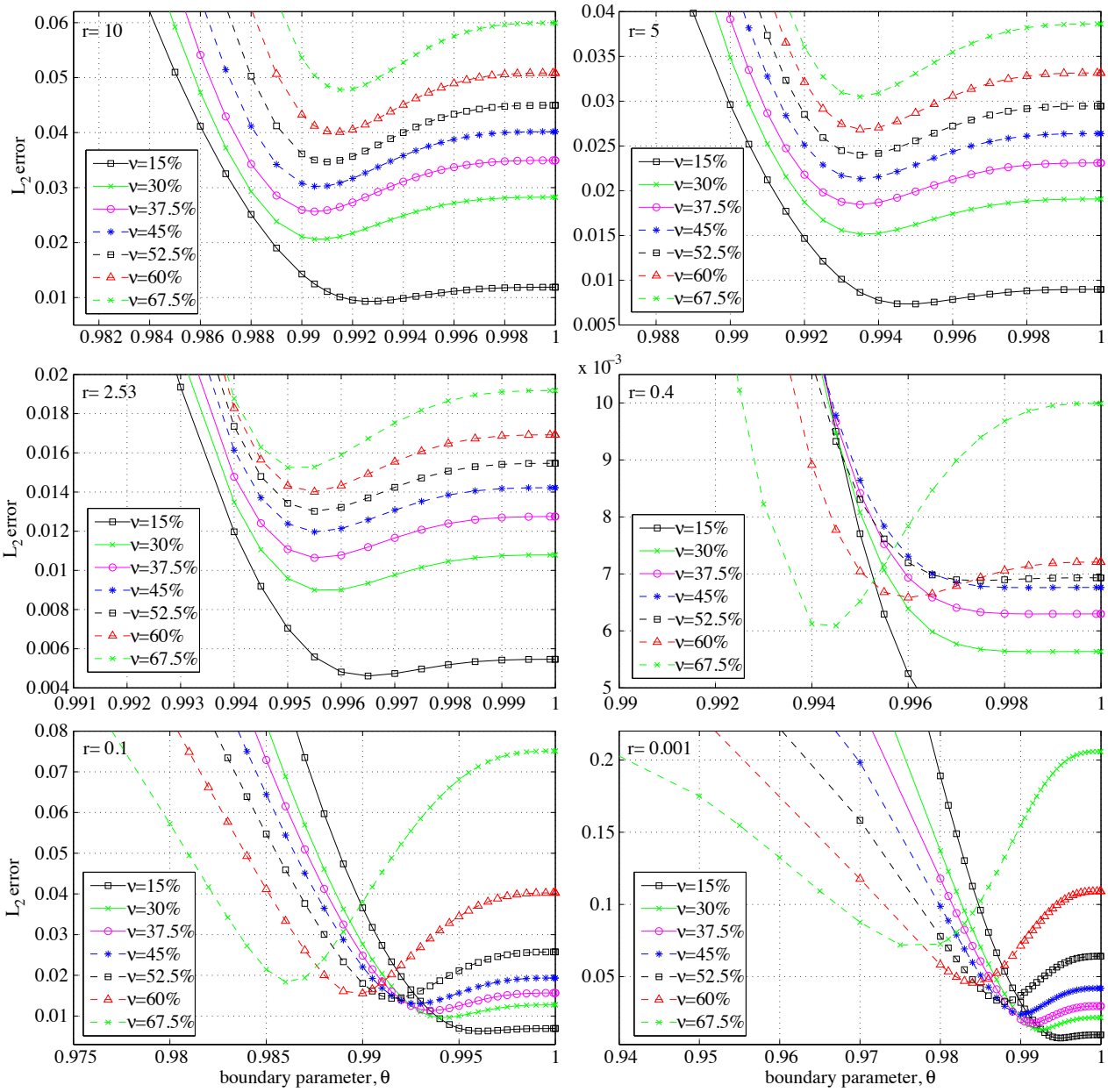

Figure 11: The L_2 error of the VME model as a function of the boundary parameter, θ.

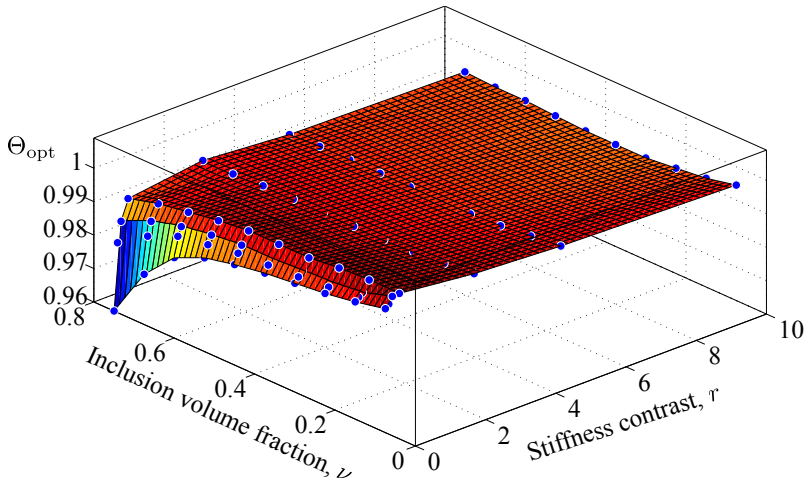

Figure 12: Optimal boundary parameter as a function of the microstructural characteristics.

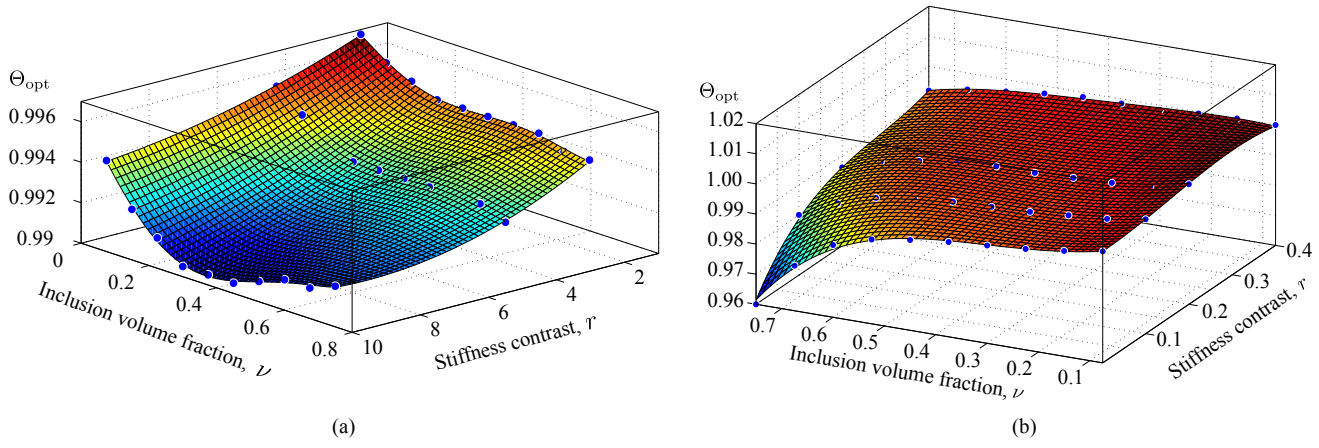

Figure 13: The parametric model of the optimal boundary parameter as a function of microstructural characteristics.

using simulation of the three-inclusion composite response. The microstructure geometry is set as constants for all simulations (i.e., $\nu = 0.25$). Figure 14 shows the variation of the modeling error compared to the DNS as a function of the boundary parameter, θ for various stiffness contrasts ranging four orders of magnitude. The error characteristics follow a similar trend to that of a single inclusion model. For high stiffness contrasts (i.e., $1 \ll r$ or $r \ll 1$) the optimal boundary parameter provides a significant improvement to the solution accuracy, whereas the RFB approach is satisfactory for composite problems with low stiffness contrast. Figure 14 also illustrates the performance of the optimal boundary parameter model (Eq. 67). The errors computed using the boundary parameter provided by this model display higher accuracy compared to the results using the RFB functions for the entire range of stiffness contrasts.

The proposed parametric fit does not necessarily provide accurate optimal parameter prediction with arbitrary microstructures. It is perhaps reasonable to consider a similar identification methodology to obtain optimal boundary parameter function for other microstructural configurations that can be described by a set of microstructural parameters.

The performance of the proposed boundary parameters is demonstrated using periodically arranged microstructures, but the multiscale approach is also applicable to non-periodic microstructures. The boundary conditions and the overall multiscale approach is expected to work well in the presence of spatially varying and non-periodic microstructures, since no assumptions are made in the model formulation regarding microstructural periodicity. The purpose of using periodic microstructures is to ensure that, to the extent possible, the performance of the boundary conditions are isolated from other potential sources of errors and complicating factors.

5 Conclusions

In this manuscript, we presented a new variational multiscale enrichment method for diffusion and deformation problems. This method includes a new family of microscale boundary conditions of Robin type, which relax the overconstraint imposed by the residual free bubble approach (i.e., homogeneous microscale boundary conditions). The proposed boundary conditions give rise to microscale response functions, named canopy functions, which take on nonzero values along the boundary edges of the microscale problems. The field continuity between neighboring enriched domains is satisfied using the penalty method through straightforward modification of the proposed boundary conditions.

The performance of the method is assessed against direct numerical simulations in the context of diffusion and deformation problems. The new boundary conditions provide significant improvement compared to homogeneous boundaries when the boundary parameter is appropriately chosen. We offered possible choices for the boundary parameter through parametric analyses. For diffusion problems, a boundary parameter independent of the model parameters is recommended. For deformation problems, the optimal boundary parameter was found to be

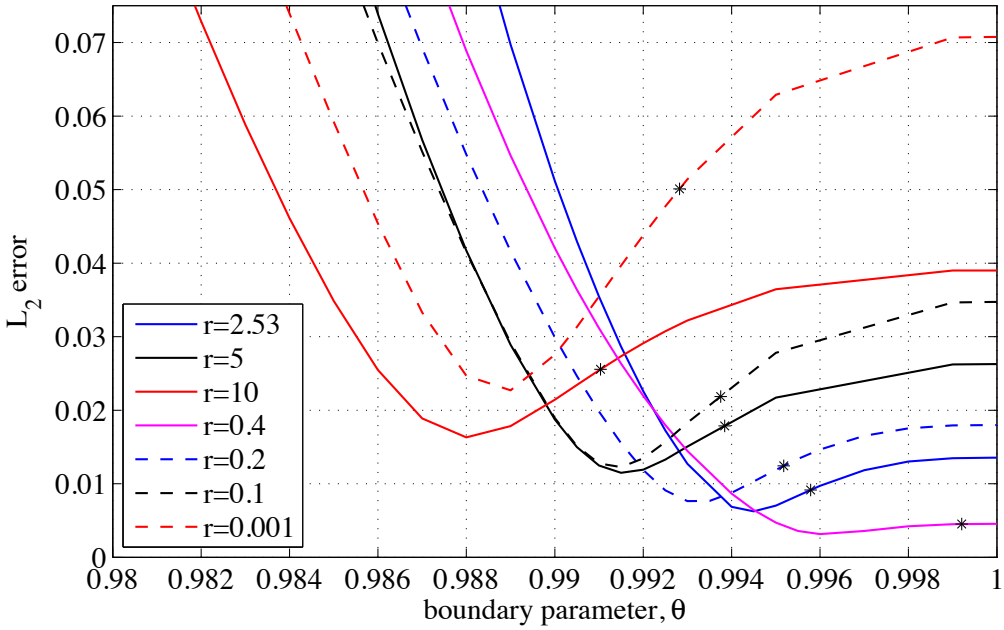

Figure 14: The L_2 error of the VME model as a function of the boundary parameter, θ in the three inclusion model. Boundary parameter based on parametric model (i.e., Eq. 67) identified as black stars.

a function of the model parameters, and an identification approach is proposed for obtaining near-optimal boundary conditions. The identification approach is verified in the context of particle-reinforced composite problems.

Several important advancements to the VME method are under development. First, this manuscript provided the implementation for 2-D problems only. The implementation of the problem will be extended to 3-D in the near future. Next, is devising efficient computational algorithms for the parallel implementation of the proposed computational methodology. While the present approach is computationally efficient compared with direct numerical simulations, analysis of large-scale three-dimensional structures will require the implementation of parallel algorithms capable of efficiently evaluating the multiscale response in view of the high computational cost of evaluating the microscale problems numerically. The parallel implementation is challenging with the new boundary conditions because of the communication between enrichment domains to ensure inter-enrichment domain continuity (no such requirement exists for the case of homogeneous boundary conditions). Third, the transport processes into mechanical systems typically cause microcracking and inelastic processes. The extension of the proposed methodology to incorporate the presence of inelastic processes and fracture within the boundary region is important for realistic simulations that model surface degradation problems, such as the response of titanium structures subjected to extreme environments. Finally, it is desirable to adaptively identify and evolve the boundary region throughout the simulation process and automatically enrich/un-enrich subdomains as a function of the response. Such an adaptive strategy is particularly important for accurate and efficient modeling of evolving

failure phenomena. Our near term efforts will therefore include extending the proposed multi-scale computational framework to parallel implementation for three-dimensional and inelastic problems.

6 Acknowledgements

The author gratefully acknowledges the AFRL Structural Sciences Center (Contract No: BY11-006SP through High Performance Technologies, Inc.) for funding and support of this research.

References

[1] O. Lloberas-Valls, D. J. Rixen, A. Simone, and L. J. Sluys. Domain decomposition techniques for the efficient modeling of brittle heterogeneous materials. *Comput. Methods Appl. Mech. Engrg.*, 200:1577–1590, 2011.

[2] J. Fish. The s-version of the finite element method. *Computers & Structures*, 43:539–547, 1992.

[3] C. A. Duarte and D. J. Kim. Analysis and applications of a generalized finite element method with global–local enrichment functions. *Comput. Methods Appl. Mech. Engrg.*, 197:487–504, 2008.

[4] T. J. R. Hughes. Multiscale phenomena: Green's functions, the dirichlet-to-neumann formulation, subgrid-scale models, bubbles and the origins of stabilized methods. *Comp. Meth. Appl. Mech. Engng.*, 127:387–401, 1995.

[5] T. J. R. Hughes, G. R. Feijoo, and J. B. Quincy. The variational multiscale method - a paradigm for computational mechanics. *Comp. Meth. Appl. Mech. Engng.*, 166:3–24, 1998.

[6] K. Garikipati and T. J. R. Hughes. A variational multiscale approach to strain localization formulation for multidimensional problems. *Comp. Meth. Appl. Mech. Engng.*, 188:39–60, 2000.

[7] T. J. R. Hughes and G. Sangalli. Variational Multiscale Analysis: the Fine-scale Green's Function, Projection, Optimization, Localization, and Stabilized Methods. *SIAM Journal on Numerical Analysis*, 45(2):539, 2007.

[8] T. Arbogast. Analysis of a Two-Scale, Locally Conservative Subgrid Upscaling for Elliptic Problems. *SIAM Journal on Numerical Analysis*, 42:576, 2004.

[9] T. Arbogast. Implementation of a locally conservative numerical subgrid upscaling scheme for two-phase Darcy flow. *Comput. GeoSci.*, 6:453–481, 2002.

[10] C. Oskay. Variational multiscale enrichment for modeling coupled mechano-diffusion problems. *Int. J. Numer. Meth. Engng.*, 89:686–705, 2012.

[11] C. Baiocchi, F. Brezzi, and L. P. Franca. Virtual bubbles and the galerkin/least-squares method. *Comp. Meth. Appl. Mech. Engng.*, 105:125–142, 1993.

[12] F. Brezzi, L. P. Franca, T. J. R. Hughes, and A. Russo. $b = \int g$. *Comp. Meth. Appl. Mech. Engng.*, 145:329–339, 1997.

[13] R. Juanes and F.-X. Dub. A locally conservative variational multiscale method for the simulation of porous media flow with multiscale source terms. *Comput. Geosci.*, 12:273–295, 2008.

[14] D. Markovic and A. Ibrahimbegovic. On micro–macro interface conditions for micro scale based FEM for inelastic behavior of heterogeneous materials. *Comput. Methods Appl. Mech. Engrg.*, 193:5503–5523, 2004.

[15] A. Hund and E. Ramm. Locality constraints within multiscale model for non-linear material behaviour. *Int. J. Numer. Meth. Engng.*, 70:1613–1632, 2007.

[16] J. Fish and R. Fan. Mathematical homogenization of nonperiodic heterogeneous media subjected to large deformation transient loading. *Int. J. Numer. Meth. Engng.*, 76:1044–1064, 2008.

[17] E. W. C. Coenen, V. G. Kouznetsova, and M. G. D. Geers. Novel boundary conditions for strain localization analyses in microstructural volume elements. *Int. J. Numer. Meth. Engng.*, 90:1–21, 2012.

[18] C. Oskay and G. Pal. A multiscale failure model for analysis of thin heterogeneous plates. *Int. J. Damage Mechanics*, 19:575–611, 2010.

[19] J. A. Evans, T. J. R. Hughes, and G. Sangalli. Enforcement of constraints and maximum principles in the variational multiscale method. *Comput. Methods Appl. Mech. Engrg.*, 199:61–76, 2009.

[20] G. Scovazzi and B. Carnes. Weak boundary conditions for wave propagation problems in confined domains: Formulation and implementation using a variational multiscale method. *Comput. Methods Appl. Mech. Engrg.*, 221-222:117–131, 2012.

[21] F. Brezzi and M. Fortin. *Mixed and hybrid finite element methods*, volume 15 of *Springer Series in Computational Mathematics*. Springer-Verlag, 1991.

[22] J. Fish and Z. Yuan. Multiscale enrichment based on partition of unity. *Int. J. Numer. Meth. Engng.*, 62:1341–1359, 2005.

[23] C. Oskay. Two-level multiscale enrichment methodology for modeling of heterogeneous plates. *Int. J. Numer. Meth. Engng.*, 80:1143–1170, 2009.

[24] H. P. Langtangen and A. Tveito, editors. *Advanced Topics in Computational Partial Differential Equations*. Lecture Notes in Computational Science and Engineering. Springer, 2003.

[25] H. P. Langtangen. *Computational Partial Differential Equations: Numerical Methods and Diffpack Programming*. Springer, 2003.

[26] C. Oskay and M. Haney. Computational modeling of titanium structures subjected to thermo-chemo-mechanical environment. *Int. J. Solids Struct.*, 47:3341–3351, 2010.